FLAT QUARTZ-CRYSTAL X-RAY SPECTROMETER

FOR NUCLEAR FORENSICS APPLICATIONS

A Thesis

by

ALISON VICTORIA GOODSELL

Submitted to the Office of Graduate Studies of
Texas A&M University
in partial fulfillment of the requirements for the degree of

MASTER OF SCIENCE

August 2012

Major Subject: Nuclear Engineering

Flat Quartz-Crystal X-Ray Spectrometer for Nuclear Forensics Applications

FLAT QUARTZ-CRYSTAL X-RAY SPECTROMETER

FOR NUCLEAR FORENSICS APPLICATIONS

A Thesis

by

ALISON VICTORIA GOODSELL

Submitted to the Office of Graduate Studies of
Texas A&M University
in partial fulfillment of the requirements for the degree of

MASTER OF SCIENCE

Approved by:

Chair of Committee,	William S. Charlton
Committee Members,	John W. Poston, Sr.
	Arnold Vedlitz
Head of Department,	Yassin A. Hassan

August 2012

Major Subject: Nuclear Engineering

ABSTRACT

Flat Quartz-Crystal X-ray Spectrometer for Nuclear Forensics Applications.

(August 2012)

Alison Victoria Goodsell, B.S., California Polytechnic State University, San Luis Obispo

Chair of Advisory Committee: Dr. William S. Charlton

The ability to quickly and accurately quantify the plutonium (Pu) content in pressurized water reactor (PWR) spent nuclear fuel (SNF) is critical for nuclear forensics purposes. One non-destructive assay (NDA) technique being investigated to detect bulk Pu in SNF is measuring the self-induced x-ray fluorescence (XRF). Previous XRF measurements of Three Mile Island (TMI) PWR SNF taken in July 2008 and January 2009 at Oak Ridge National Laboratory (ORNL) successfully illustrated the ability to detect the 103.7 keV x ray from Pu using a planar high-purity germanium (HPGe) detector. This allows for a direct measurement of Pu in SNF. Additional gamma ray and XRF measurements were performed on TMI SNF at ORNL in October 2011 to measure the signal-to-noise ratio for the 103.7 keV peak.

Previous work had shown that the Pu/U peak ratio was directly proportional to the Pu/U content and increased linearly with burnup. However, the underlying Compton background significantly reduced the signal-to-noise ratio for the x-ray peaks of interest thereby requiring a prolonged count time. Comprehensive SNF simulations by Stafford et al showed the contributions to the Compton continuum were due to high-energy

gamma rays scattering in the fuel, shipping tube, cladding, collimator and detector[1]. The background radiation was primarily due to the incoherent scattering of the ^{137}Cs 661.7 keV gamma. In this work methods to reduce the Compton background and thereby increase the signal-to-noise ratio were investigated.

To reduce the debilitating effects of the Compton background, a crystal x-ray spectrometer system was designed. This wavelength-dispersive spectroscopy technique isolated the Pu and U x rays according to Bragg's law by x-ray diffraction through a crystal structure. The higher energy background radiation was blocked from reaching the detector using a customized collimator and shielding system.

A flat quartz-crystal x-ray spectrometer system was designed specifically to fit the constraints and requirements of detecting XRF from SNF. Simulations were performed to design and optimize the collimator design and to quantify the improved signal-to-noise ratio of the Pu and U x-ray peaks. The proposed crystal spectrometer system successfully diffracted the photon energies of interest while blocking the high-energy radiation from reaching the detector and contributing to background counts. The spectrometer system provided a higher signal-to-noise ratio and lower percent error for the XRF peaks of interest from Pu and U. Using the flat quartz-crystal x-ray spectrometer and customized collimation system, the Monte Carlo N-Particle (MCNP) simulations showed the 103.7 keV Pu x-ray peak signal-to-noise ratio improved by a factor of 13 and decreased the percent error by a factor of 3.3.

DEDICATION

This thesis is dedicated to my friends and family for all of their support during my academic career.

ACKNOWLEDGEMENTS

I would like to thank my committee chair, Dr. William Charlton, for all of his assistance and expertise. I would like to acknowledge my committee members, Dr. John Poston and Dr. Arnold Vedlitz, for their guidance. My thanks also to Nuclear Security Science & Policy Institute staff members Claudio Gariazzo and Dr. Alexander Solodov for their help. Also, thanks to Dr. Sunil Chirayath for answering the random MCNP simulation question. I would like to acknowledge the staff and technicians at Oak Ridge National Laboratory who assisted with the spent nuclear fuel measurements in October 2011.

Thank you to my fellow graduate students in the Nuclear Engineering department and NSSPI for making my graduate experience at Texas A&M University very enjoyable.

NOMENCLATURE

ADEPT	Advanced Diagnostics and Evaluation Platform
Al	Aluminum
Ba	Barium
BU	Burnup
Cs	Cesium
GeLi	Lithium-drifted Germanium
HPGe	High-Purity Germanium
LWR	Light Water Reactor
MCNP	Monte Carlo N-Particle
NDA	Nondestructive Analysis
Np	Neptunium
ORNL	Oak Ridge National Laboratory
Pb	Lead
PWR	Pressurized Water Reactor
Pu	Plutonium
TAMU	Texas A&M University
TMI	Three Mile Island
U	Uranium
W	Tungsten
XRF	X-ray Fluorescence

TABLE OF CONTENTS

Page

LIST OF FIGURES

Page

Page

Page

LIST OF TABLES

Page

1. INTRODUCTION

The ability to quickly and accurately measure the bulk plutonium (Pu) content in spent nuclear fuel (SNF) is needed to improve the nuclear forensics capabilities in the United States. If an unidentified SNF rod was interdicted, scientists would need to quickly determine characteristics of the material, such as its composition, age and origin.

Self-induced x-ray fluorescence (XRF) is a passive, non-destructive assay (NDA) technique used to directly measure the Pu content in SNF. Measuring the ratio between the uranium (U) and Pu x-ray peaks emitted from SNF provides information about the relative concentration of U and Pu[1,2]. If the total U mass is known, the bulk Pu mass can be calculated using the ratio.

The research presented here describes an optimized and customized design of a flat quartz-crystal x-ray spectrometer for measuring the Pu and U XRF in SNF for quantifying the bulk Pu content. The use of a flat-quartz crystal to diffract incident x rays presents a simple, repeatable and passive method for measuring a narrow energy band of radiation from an energetically heterogeneous source.

This section presents previous work in quantifying the Pu content in SNF, provides background information on the Pu production in PWR fuel, the physics of XRF, the history and science of crystal diffraction and the use of wavelength dispersive spectroscopy to detect precise photon energies. Section 2 presents the procedure and

---

This thesis follows the style of *Nuclear Science & Engineering*.

analysis of the October 2011 TMI SNF XRF measurement campaign at ORNL and the applicability of using a flat crystal x-ray spectrometer when measuring photons from SNF. Section 3 delves into the design of the flat-quartz crystal used in the spectrometer system. Section 4 details the design and optimization of the customized collimator. Section 5 describes the simulations performed using MCNP for modeling the diffraction and collimation of the experiment for multiple source definitions. Section 6 covers conclusions and future work involving the use of a crystal spectrometer for XRF detection.

1.1 Objective

The ability to quickly and accurately quantify the bulk Pu content within SNF is critical to nuclear forensics. The Pu content in SNF can be acquired through the NDA method of detecting self-induced XRF from the Pu in the fuel. By taking the ratio of the Pu and U XRF peaks, the total Pu content in the fuel can be determined if the total U mass is known. However, during conventional photon spectroscopy, the characteristic Pu x-ray peak of interest is obscured by background[2]. The objective of this thesis was to show that the proposed crystal spectrometer design significantly increases the signal-to-noise ratio of the Pu and U XRF peaks obtained from photon spectroscopy of SNF by decreasing Compton interactions in the detector. This was demonstrated through the design of a flat quartz-crystal x-ray spectrometer and by performing proof-of-concept simulations. The ability of the spectrometer system to isolate gamma and x rays in the

energy range of interest (80-125 keV) while blocking high energy photons from reaching the detector was evaluated.

1.2 Previous Work

1.2.1 Nuclear Forensics

Nuclear forensics is the analysis of illicit nuclear materials recovered by an interdiction or from post-detonation debris to determine the type of material, its origin and the identity of the accountable party[3]. The United States uses its nuclear forensics capabilities, in parallel with traditional forensics and the intelligence community, to deter nuclear capable states from attacking and/or assisting terrorist organizations in acquiring a nuclear device. This deterrence depends on being able to identify the responsible culprit and ensuring retribution against any adversary who attacks. Since nuclear forensics is vital for attribution and thus deterrence, the US must continuously improve its forensics capabilities.

The ability to determine the plutonium content in SNF is needed for nuclear forensics applications to ascertain fuel characteristics that could lead to identifying its origin. The bulk Pu content within a SNF rod, in conjunction with other passive NDA signatures, can provide vital information on the fuel history. NDA measurements allow scientists to determine the type of reactor in which the fuel was irradiated, burnup, initial enrichment, cooling time and, to some extent, the reactor power history. This process is demonstrated in Figure 1.

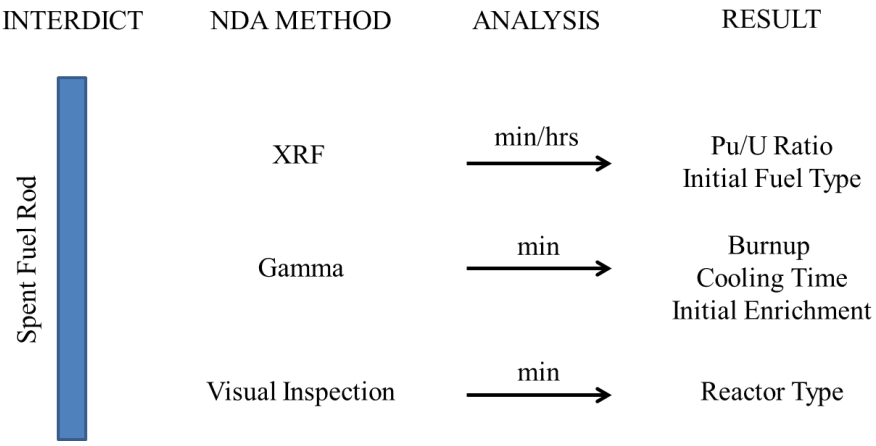

Figure 1. Nuclear forensics NDA techniques used to determine pertinent characteristics of an interdicted spent fuel rod.

The threat of a nuclear attack on US soil is a low probability and high consequence event. The capability to deter nuclear terrorism relies partly on the scientific community's confidence in their ability to quickly and accurately ascertain the responsible adversary.

1.2.2 Using XRF to Quantify the Pu Content in SNF

In the early 1980s, A.V. Bushuev suggested using the elemental Pu and U XRF excited by fission product emissions in fast reactor fuel to determine the Pu to U content ratio[4]. Bushuev stated that after some study, the 98.4 keV U x ray and the 103.7 keV Pu x ray could be detected and resolved using a lithium-drifted germanium (GeLi) spectrometer. He identified several factors specifically for a fast reactor which could affect the XRF measurement results, including an "inadequate distribution of U and Pu

along the radius of the fuel element" due to the low $^{238}U(n,\gamma)$ radiative capture cross section for fast neutrons and the different absorption coefficients of the Pu and U characteristic x rays[4]. Also he noted that a semiconductor spectrometer with an energy resolution of less than 0.7 keV in the energy range of interest was needed[4]. Bushuev's application was specifically for fast reactor fuel, which could contain up to 40% Pu while for LWR UO_2 fuel the Pu content is ~1%.

In 1998, C. Rudy performed photon measurements for safeguards verification on Kazakhstan's BN-350 fast breeder reactor fuel that had been cooled for 5-10 years[5]. The measurements were taken using a 3-m long collimator through a hot cell wall with a 25% efficient HPGe detector. Rudy's photon measurement analysis correlated the Pu and U x-ray fluxes emitted from the fuel to the bulk Pu/U mass ratio. The flux ratio related the peak areas, branching ratios, detection efficiencies and fluorescent yields of the 98.4 keV U x ray and the 103.7 keV Pu x ray[5]. For the two x rays, the branching ratios and fluorescent yields were found to be nearly identical such that the ratio of the Pu/U flux could be simplified to a ratio of the peak areas multiplied by a relative efficiency factor[5]. The relative efficiency was calculated using the peak areas of the five U K-shell x rays[5]. Rudy's approximation was contingent upon some assumptions, including that the spatial distribution of the Pu and U was the same and that attenuation from the fuel and cladding for both x-ray energies was identical. Another assumption was that the Pu and U were identically excited by the background radiation flux[5]. Overall, Rudy concluded that the Pu and U XRF could be observed from photon

measurements and, with additional research, could be used to quantify the elemental Pu content using the Pu to U ratio[5].

However, not all of Rudy's assumptions apply to a thermal reactor. Due to ^{238}U absorption of epithermal neutrons, more neutrons are captured before reaching the interior of the fuel pellet[5]. Thus, Pu is preferentially produced at the surface edge of the fuel pin. Also, the Pu concentration depends on the fuel burnup. Figure 2 shows the expected Pu concentration in PWR SNF as a function of radial position and burnup calculated using TransLat[6,7]. The Pu concentration increases with increasing fuel rod radius. To properly quantify the bulk Pu content in spent PWR UO_2 fuel, the radial Pu distribution must be known. From additional NDA measurements of the $^{134}Cs/^{137}Cs$ activity ratio, the fuel burnup can be calculated and used to approximate the expected radial Pu distribution[1].

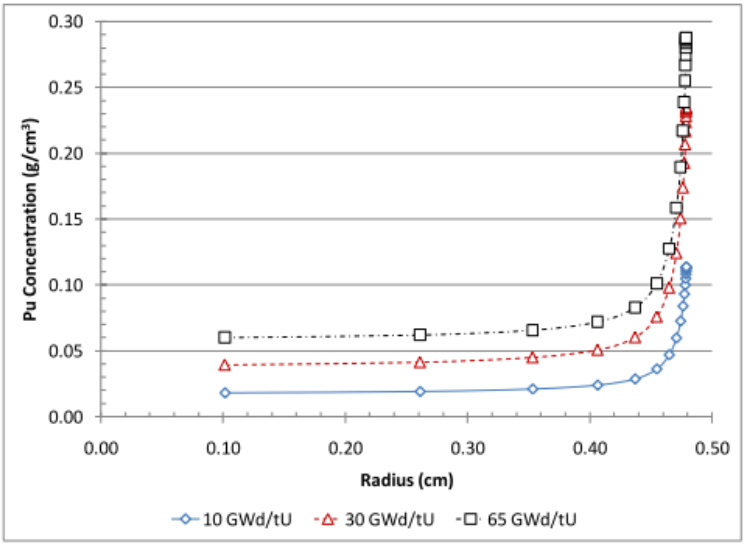

Figure 2. Pu concentration versus radial position for PWR SNF at several burnups[7]

1.2.3 Self-Induced XRF from SNF to Predict the Pu/U Content

Former Texas A&M University graduate student, Alissa Stafford's master's thesis, "Spent Nuclear Fuel Self-Induced XRF to Predict Pu to U Content," used experimentally-obtained PWR SNF XRF spectra along with simulation of XRF measurements using comprehensive MCNP modeling of SNF to determine the feasibility of quantifying the Pu content by taking the ratio of the detected Pu to U XRF peaks[1]. Overall, she found that it was possible to measure the Pu and U self-induced XRF from low-enriched UO_2 PWR spent nuclear fuel[1]. In addition, she determined that the PWR spent fuel simulations accurately modeled the primary fission product high-energy emissions and the secondary XRF emissions[1]. Her models also showed large contributions to the Compton background caused by incoherent scattering of high-energy gamma radiation in the fuel, shipping tube, cladding, collimator and detector[1]. This led to the necessity of unacceptably long count times to accumulate significant counting statistics[1].

1.3 Theory

1.3.1 Pu Production in PWR Fuel

Thermal nuclear reactor fuel is typically composed of uranium dioxide (UO_2). The U is enriched to some percentage of uranium-235 (^{235}U) depending on the type of reactor. For a PWR, the fuel is generally enriched to approximately 4% ^{235}U from natural U, which has a composition of 99.27% ^{238}U, 0.72% ^{235}U and 0.0054% ^{234}U. During standard operation of a thermal nuclear power plant, the ^{238}U, which still

comprises the majority of the uranium mass in the reactor, is more likely to capture neutrons, and thus begin the transmutation process to ^{239}Pu, than to undergo fission (Fig. 3). The ^{238}U microscopic radiative capture cross section is much larger than the ^{238}U fission cross section for thermal or epithermal neutrons[8].

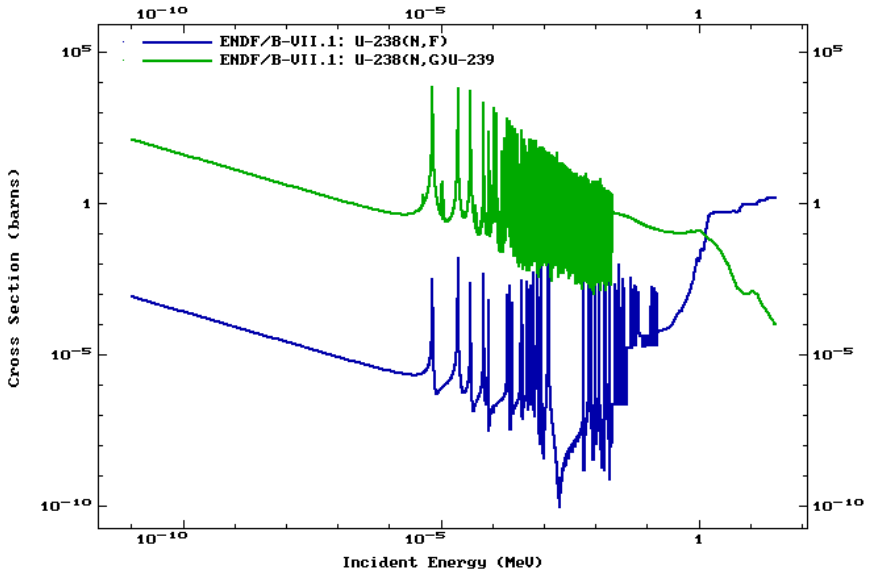

Figure 3. The microscopic fission (n,f) and radiative (n,γ) cross section versus neutron energy plots for ^{238}U [8]

The nuclear reaction that produces the fissile ^{239}Pu from ^{238}U is:

$$^{238}_{92}U + n \rightarrow ^{239*}_{92}U \xrightarrow{\beta-} ^{239}_{93}Np \xrightarrow{\beta-} ^{239}_{94}Pu \quad (1)$$

Once ^{238}U captures a neutron, it becomes an excited ^{239}U atom. Uranium-239* shortly undergoes β- decay (24 min half-life) to ^{239}Np. It undergoes a second β- decay to become the fissile ^{239}Pu isotope. Figure 4 shows the additional transmutation reactions that produce the Pu vector in a reactor.

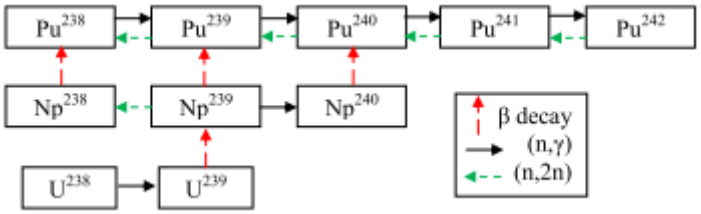

Figure 4. Pu vector buildup from ^{238}U in a nuclear reactor[1]

Figure 5 shows how the Pu isotopes buildup in the fuel with increasing burnup (BU). While ^{239}Pu is produced essentially immediately, the other Pu isotopes build up more slowly at first[9]. By the end of the reactor fuel irradiation period, which lasts several years in a PWR, a substantial amount of Pu is created such that the SNF is comprised of 1-2% Pu, with the remaining fuel composed of depleted U (95%) and fission products (3%).

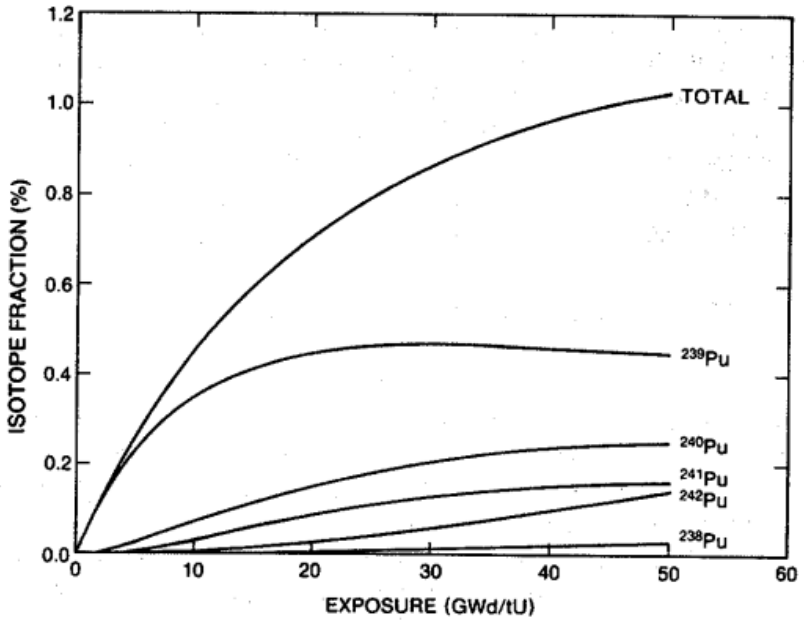

Figure 5. The Pu isotopic fraction buildup with increasing burnup in a PWR[9]

In SNF, even after prolonged cooling, high-energy photons, neutrons and beta particles produced by the decay of fission products create heat and high radiation levels. The most significant of these fission products is ^{137}Cs (30.1 year half-life) which decays to ^{137m}Ba. Ba-137m quickly decays (2.55 min half-life) to stable ^{137}Ba, emitting a 661.7 keV gamma-ray. Cesium-137 and other fission products create a constant background of radiation which excites XRF from elements within the fuel, including U and Pu. Since the decay of fission products in the SNF causes the XRF within the fuel and no additional radiation is introduced to the system, this is known as passive, or self-induced, XRF.

1.3.2 X-ray Fluorescence

When an atom is ionized by a high-energy photon such that an electron is ejected, a higher orbital electron falls into the vacancy or "hole." This transition results in XRF, the emission of a characteristic x ray with an energy equal to the difference of the two binding energies. Depending on the orbital levels undergoing the electron ejection and transition, XRF has strict nomenclature. If the ejected electron originated in the innermost K-shell of the atom, when a higher orbital electron dropped into the electron vacancy, it would correspond to a K transition. If the transitioning, or "falling," electron originated from the L-shell or M-shell, the characteristic x ray would correspond to a K_α or K_β emission, respectively (Fig. 6). Transitions between higher orbital shells (L, M, N, etc.) occur less frequently and emit characteristic x rays at lower energies than the K-shell x rays.

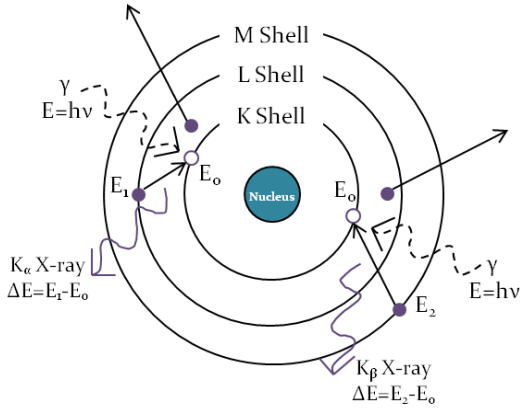

Figure 6. Simplified atomic diagram of XRF

Characteristic x-ray energies for most elements are known from previous experiments. The XRF lines of interest for Pu and U range from approximately 95-120 keV (Table I)[9]. While these energies are relatively low compared to the ^{137}Cs gamma-rays, these are very high for typical x-ray energies.

Table I. Uranium and plutonium characteristic x-ray data[9]

X ray	Energy (keV)		Relative Intensity	
	Uranium	Plutonium	Uranium	Plutonium
$K_{\alpha 1}$	98.44	103.76	100	100
$K_{\alpha 2}$	94.67	99.55	61.9	62.5
$K_{\beta 1}$	111.30	117.26	22.0	22.2
$K_{\beta 2}$	114.50	120.60	12.3	12.5
$K_{\beta 3}$	110.41	116.27	11.6	11.7

1.3.3 Crystal Structure

Crystallography, the study of crystalline structure, has been pursued extensively for hundreds of years[10]. Crystallography is important in a variety of scientific disciplines including physics, biology, chemistry, engineering and geology. A fundamental concept in the study of crystals is the idea that a crystal is composed of identical copies of a unit cell stacked in the same orientation[10]. In the early 1800s, British mineralogist William H. Miller developed an indexing method to compactly describe the crystal axes using a set of three integers (*h k l*). The Miller indices created a notation system to label planes and directions in crystal lattices[10].

Crystallographic methods were developed by scientists to determine the crystal interplanar structure and spacing for many crystal materials[10]. Depending on how a crystal was oriented when it was cut, the Miller index and the effective interplanar spacing were changed[11].

1.3.4 Laue's Method

In 1914, German physicist Max von Laue won the Nobel Prize in Physics for discovering x-ray diffraction by crystals[11]. Laue theorized that photons, with wavelengths on the scale of the interplanar spacing of a crystal lattice structure, would interact with the bound atoms and be coherently scattered. The coherently scattered x-rays would possess the same wavelength as the initial photons due to constructive interference from the coherent diffraction.

Laue initially developed this diffraction technique for crystallography, the science of analyzing crystalline structure. Only months after first theorizing x-ray diffraction through crystals, Laue and several collaborators designed an experimental test. The x-ray generating bulb was supplied by Wilhelm Rontgen, the discoverer of x rays, and the diffracting crystal was produced by Paul Heinrich Ritter von Groth, a leading crystallographer of the time[11]. The experimental setup consisted of a collimated x-ray beam directed onto a copper sulfate crystal (Fig. 7). Photographic plates on which the diffracted x-ray beams would be recorded were placed at different distances and directions around the crystal.

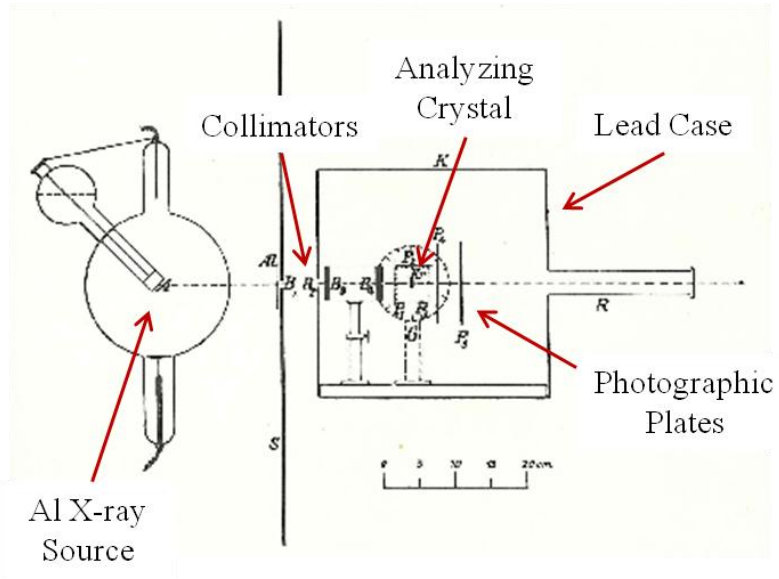

Figure 7. The original experimental setup investigating x-ray diffraction by a crystal[12]

Analysis of the photographic plates displayed the presence of diffracted x-ray beams emitted rectilinearly outward in all directions from the crystal. Laue developed

methodologies of determining the crystal orientation and structure by analyzing the diffracted beam patterns on the photographic plates. Originally, Laue believed his diffraction theory held only approximately but it was shown in further experiments by another scientist that Laue's equations were satisfied experimentally[11].

1.3.5 Bragg Diffraction

Laue's equations were verified by William Lawrence Bragg, a young physics student at the University of Cambridge and the son of physics professor William Henry Bragg[11]. W.L. Bragg believed that Laue's analysis of the x-ray photographs was incorrect. W.L. Bragg reexamined some of Laue's assumptions about the x-ray source and effect of the crystal structure on the incident radiation[11]. W.L. Bragg considered the crystal as a diffraction grating and showed that the diffraction spots on the photographic plates corresponded to partial reflections of the x-ray radiation from sets of parallel planes in the crystal[11]. The x-ray beam was coherently scattered by the crystal but destructive interference from the out-of-phase rays allowed only x rays with a path difference equal to a multiple of the x-ray wavelength to be conserved[12].

Using additional diffracting crystals, W.L. Bragg proved that the laws of diffraction were obeyed and could be presented in a compact equation. Bragg's law of diffraction is given by:

$$n\lambda = 2dsin\theta \quad (2)$$

where λ is the photon wavelength, d is the crystal interplanar spacing, θ is the Bragg angle of diffraction and n is a positive integer set equal to one. Also, as photon energy

(*E*) is related to wavelength, the Bragg angle can be easily calculated for any known x-ray energy:

$$E = {}^{hc}/_{\lambda} \quad (3)$$

where *h* is Planck's constant and *c* is the speed of light.

Thus, an array of x-ray energies and their corresponding wavelengths will each have a unique, first-order Bragg angle. If the crystal structure is known, the diffraction angles for incident x rays with known energies can be calculated. This allows for a detector to be positioned specifically for the detection of a desired photon energy. W.L. Bragg and his father were awarded the Nobel Prize in Physics for the Bragg equation in 1915[11].

1.3.6 Wavelength-Dispersive Spectroscopy

From the early experiments of Laue and the Braggs, multiple methods of resolving x rays into a spectrum were designed for wavelength-dispersive spectroscopy using crystal lattice plane diffraction[12]. Similarly to how visible white light is refracted and dispersed according to its wavelength as it passes through a prism, x rays undergo an angular separation based on their energy when diffracted by a crystal lattice. Using Bragg's law of diffraction for x rays passing through a crystal with known properties and orientation, the different x-ray energies would be reflected at unique Bragg angles.

When performing x-ray spectroscopy, the diffracting crystal is only one component of the spectrometer system. Additional necessary components include an x-ray source, a collimation system to direct a beam of radiation onto the diffracting crystal,

additional collimation behind the crystal, and a high resolution photon detector such as an HPGe.

Several physicists in the early 20th century developed unique wavelength-dispersive schemes. These methods included flat and curved crystals, different crystal materials, transmission and reflection diffraction modes, and were optimized for a range of x-ray energies. Description of these scientists' experiments follow. Additional information of these experiments can be found in references 11 and 13.

1.3.6.1 Laue/Flat Crystal

As stated previously, the Laue experimental geometry consisted of a collimated x-ray beam incident on a flat crystal (Fig. 8). The diffracted x rays were emitted conically outward from the crystal and recorded on a photographic plate oriented normal to the primary x-ray beam. A secondary beam-stop collimator blocked the original, undiffracted x-ray beam from reaching the film[11].

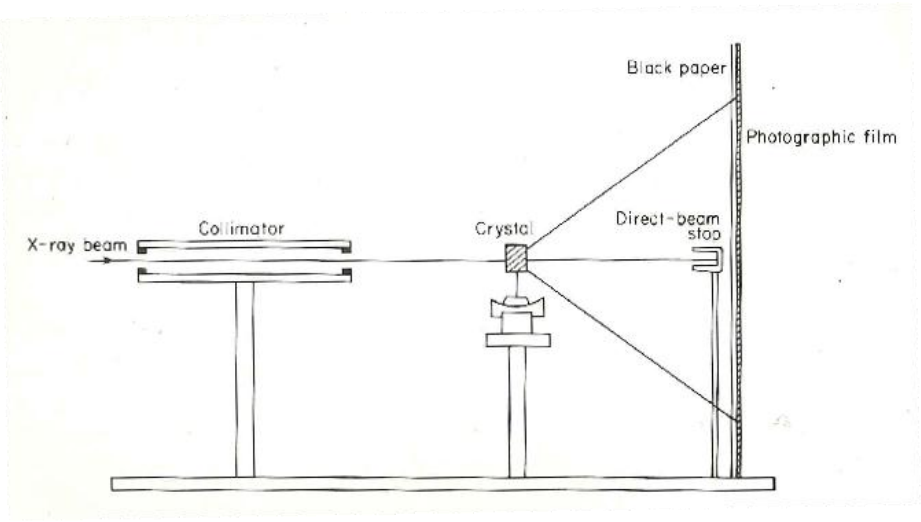

Figure 8. The experimental setup for producing Laue photographs showing the initial x-ray beam, the pinhole collimator, the analyzing crystal and the photographic film which recorded the diffraction angle of the x ray[11]

This flat crystal spectroscopy method, in which the incident x-ray beam traverses the thickness of the crystal and is diffracted according to Bragg's law, is called transmission-type. The Laue method was originally used to characterize crystalline structure but can be adapted for wavelength-dispersive spectroscopy. This can be done by using a crystal of known properties, optimized for an energy range of interest, to diffract x rays onto a high-resolution photon spectrometer, such as an HPGe detector. As the x rays are diffracted conically outward from the flat crystal, a customized collimator system can be used to isolate the desired Bragg angles which correspond to the x-ray energies of interest.

1.3.6.2 Johann and Johansson

Two early crystal x-ray spectroscopy methods were developed by physicists Johann and Johansson[13]. Originally, this wavelength-dispersive spectrometer method used photographic film to record the focused x-ray spectra. The physical position of the recorded spectra corresponded to the Bragg diffraction angle and was used to determine the energy of the diffracted x ray.

Using a bent crystal, Johann was the first to create horizontally focused x-ray spectra. For the Johann scheme, the reflecting lattice planes lie parallel to the crystal cleavage plane (Fig. 9). The crystal (K) is bent in the form of a cylinder with radius R. At the central point of the crystal (A) a tangential circle, called the Rowland circle, with radius R/2 is drawn[13]. Then due to Bragg's law of diffraction, the x rays reflect off of the curved crystal lattice at the same angle (φ) to the tangential plane. Due to the curvature of the crystal, the spectrum lines converge on the circle. However, as the bent Johann crystal does not lie perfectly on the circle, x rays reflected furthest from the crystal center are not perfectly focused on the photographic film[13]. If the angular aperture (θ) of the crystal is small, the Johann crystal's focusing ability improves. Also, the Johann method can only be used for low energies corresponding to large φ ($> 20°$). This correlation is due to the smaller the wavelength, the smaller the reflection angle φ. The shallower the reflection angle, the greater the line width which decreases the resolving power on the photographic film[13].

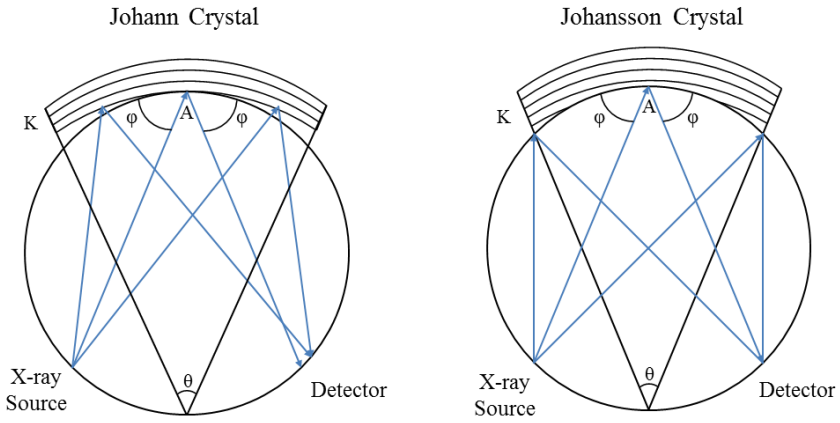

Figure 9. The Johann and Johansson schemes for wavelength dispersive spectroscopy[13]

Johansson improved upon the Johann curved crystal focusing design (Fig. 9). His method was to polish a single crystal piece into a thin plate and then bend it to form a circular cylinder with radius R[13]. After polishing, the atoms lie on planes parallel to a tangential plane at the crystal midpoint (A). The plate is then bent again to form the surface of a circular cylinder with radius R/2. This allows for the entire crystal plate to lie on the tangential circle and provides an exact focus regardless of θ. The main difficulty with the Johansson method is the crystalline plate preparation. The plate must undergo both polishing and bending to form the circular cylinder. The preparation process requires the crystal to be heated, stretched, twisted and bent, reheated, formed around a circular cylinder with radius R, cooled and then bent again to radius R/2 [13]. The process requires expertise, high accuracy and large expense.

1.3.6.3 Cauchois Method

In the mid-1930s, French physicist Yvette Cauchois was the first to design a transmission-type focusing crystal spectrometer[14]. In her design, the x-ray source is positioned on the convex side of a single crystal plate (K) bent to form a circular cylinder surface with radius R. The x rays are reflected by lattice planes that lie perpendicular to the crystal plate surface. The planes of atoms are spread out "fanwise" along radii OB, OA and OC (Fig. 10)[13]. Thus when x rays pass through the Cauchois crystal, they are diffracted by the angled lattice to Bragg's angle and focused onto a detector. The transmitted beam also converges to a point on the tangential circle. The Cauchois method suffers from some defocusing due to diffraction on the furthest edges of the crystal plate. This can be reduced by limiting the width of the incident beam using a collimator. Also, the Cauchois crystal is useful for higher energy x-ray diffraction as the crystal, depending on its thickness, absorbs low energy photons.

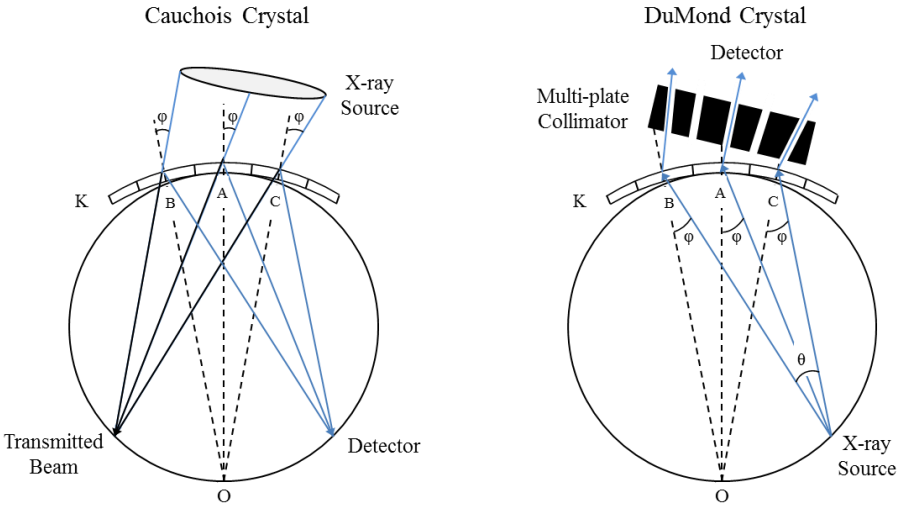

Figure 10. The Cauchois and DuMond transmission-type crystal x-ray spectrometer schemes[13,14]

1.3.6.4 DuMond Method

In the late-1940s, J.W.M. DuMond developed another transmission-type x-ray spectrometer by reversing the Cauchois geometry[15]. In the DuMond scheme, an x-ray point source was situated on the tangential Rowland circle and directed onto the concave side of a thin crystal plate (Fig. 10). As with the Cauchois crystal, the reflecting planes of the DuMond crystal were perpendicular to the crystal surface. Due to the crystal curvature, after the x rays pass through the crystal plate and are diffracted, they continue to diverge. Using a multi-plate, Soller angled collimator, the x rays of interest, based on their Bragg diffraction angle, can be isolated. The transmitted, undiffracted x-ray beam is blocked by the collimator[13]. DuMond performed many gamma spectroscopy experiments to measure the absolute photon energies from a variety of radionuclides[15].

Overall, one drawback to the focusing spectrometer system is maintaining the required geometry. In the Johann, Johansson, Cauchois and DuMond designs, special care must be taken to precisely orient the x-ray source, crystal and detector on the tangential Rowland circle. Also, the bending required for the curved crystals limits their applicability for experiments requiring different geometries and increases costs. For a portable detector to be useful, it must be able to adapt to different location constraints.

1.3.6.5 Multilayer X-ray Mirrors

Another form of wavelength-dispersive spectroscopy being investigated is the multilayer x-ray mirror[16]. Scientists at Lawrence Livermore National Laboratory are currently studying the potential use of a low-grazing angle x-ray mirror for use in astrophysics but with potential applications in nuclear safeguards and forensics. These mirrors are created by depositing very thin layers of specially chosen materials to reflect particular photon energies. Depositing multiple layers acts to decrease x-ray absorption by the material and thereby increase the reflection efficiency of the mirror. The thin layers act as interplanar spacings (*d*) such that incident x rays are diffracted according to Bragg's law (Fig. 11). Also, by varying the interplanar spacing, the Bragg equation can be satisfied for a range of x-ray energies[17].

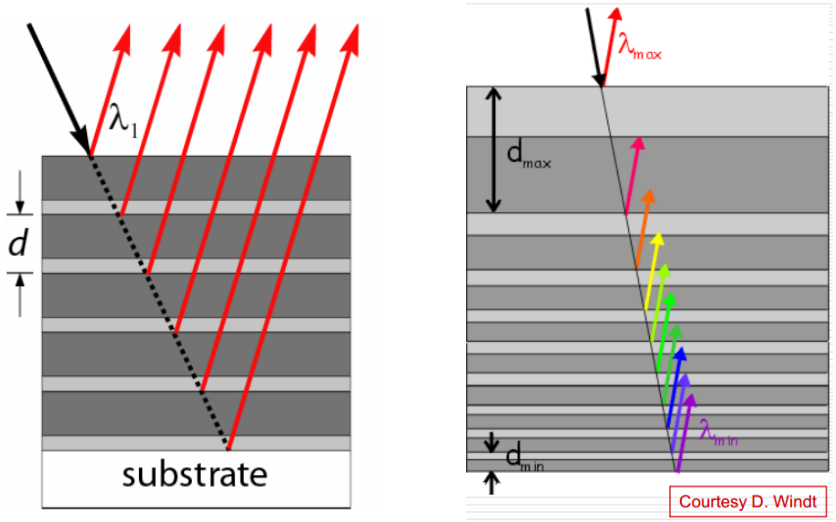

Figure 11. Multilayer x-ray mirrors offer another type of wavelength-dispersive spectroscopy technique[16,17]

2. SPECTROMETER MEASUREMENTS & DESIGN

The following sections detail the October 2011 SNF measurement campaign at ORNL and the applicability for measuring self-induced Pu and U XRF from SNF using a crystal x-ray spectrometer.

2.1 October 2011 TMI SNF Measurement Campaign

In October 2011, researchers from Texas A&M University (TAMU) participated in SNF photon measurements at ORNL using Three Mile Island (TMI) spent fuel. Both high- and low-energy photon measurements were recorded using two HPGe detectors. The SNF photon measurements for three spent fuel rods were performed in the Irradiated Fuels Examination Laboratory with the assistance of ORNL staff. Previous SNF measurements had been performed with TAMU participation in May and July 2008 and January 2009.

The TMI fuel rod D5 from assembly NJ05YU had been partitioned into several shipping tubes: 616A, 616B, 616CD and 616E[1]. Photon measurements were taken of the 616B D5 TMI SNF rod. The TMI spent fuel rod analyzed was from a PWR with a nominal burnup of 50 GWd/MTU and an initial enrichment of 4% ^{235}U [1]. The fuel rod originated from an assembly which had failed during operation due to substantial boron crud buildup[1]. In October 2011, the TMI fuel had been out of the reactor for approximately 16 years. However, due to the long-lived fission products, the fuel was still highly radioactive. The fuel was inside the hot cell and remained there for the

duration of the measurements. ORNL technicians operated mechanical manipulators, or claws, to accurately position the spent fuel rods inside the hot cell (Fig. 12).

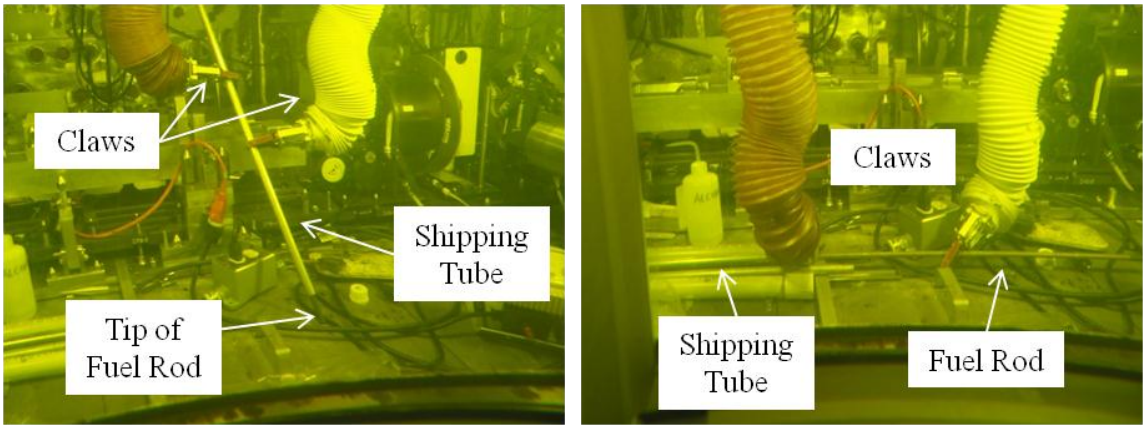

Figure 12. The ORNL technicians removed the TMI SNF from its shipping tube using the claws inside of the hot cell

The photon measurements on the TMI SNF were performed using a stainless steel collimator built into the hot cell wall (Fig. 13). Directly in front of the spent fuel, the collimator diameter was 3 cm. The collimator then narrowed to a pinhole with a diameter of 0.3 cm[1]. The stainless steel collimator was 167 cm (65.75") in length with the end inside of the hot cell approximately 20.3 cm (8") from the fuel rod surface. An extension collimation piece on the outside of the wall was 31.1 cm (12.25") long. The HPGe detector was placed within millimeters of the collimator extension. Thus the entire distance from the fuel rod to the detector was 218.4 cm (86")[1].

Figure 13. HPGe detector SNF photon measurement through the hot cell wall using the stainless steel collimator

Once the fuel rod was moved into the hot cell and the shipping tube was removed, the technicians placed the rod on a precision positioning system called the Advanced Diagnostics Evaluation Platform (ADEPT) (Fig. 14). Using a digital control system, the ADEPT system measured the length of the fuel rod such that repeatable lateral positions measurements could be taken. The ADEPT system was designed and manufactured by ORNL staff. For the first two days of photon measurements, the ADEPT system worked very well. However on the third day, the system consistently malfunctioned such that the lateral position information was corrupted for the final measurements.

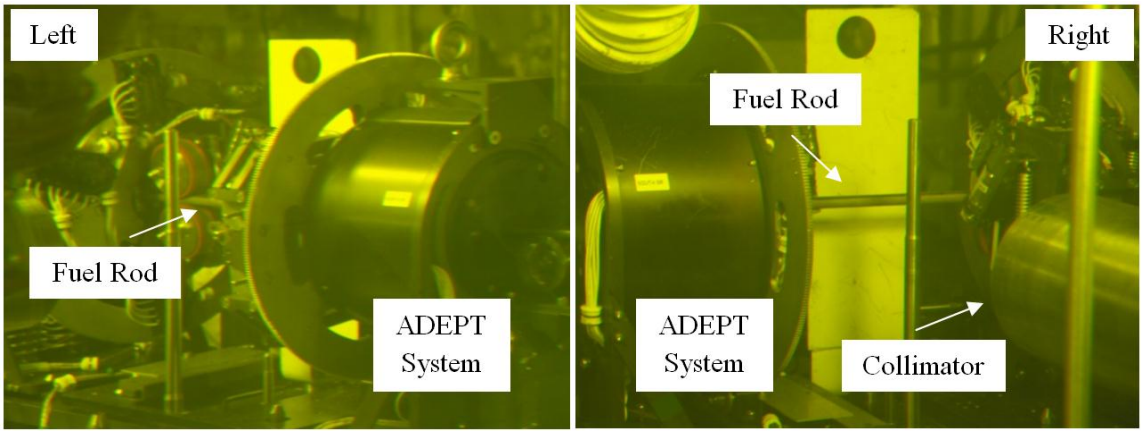

Figure 14. TMI fuel rod inserted into the ADEPT positioning system directly in front of the collimator inside of the hot cell

Two HPGe detectors, a coaxial and a planar detector, were used for the TMI SNF photon measurements. The coaxial (coax) detector was a broad-energy detector with a 25-mm thick crystal and a composite carbon window. The coax was used for high-energy gamma measurements. Two high-energy measurements were taken simultaneously with the coaxial detector by using two multi-channel analyzers (MCA). The MCA settings used are listed in Table II. One coaxial MCA was set to record photon energies from 0-2300 keV (COAX_LO) and the other from 0-3500 keV (COAX_HI). The planar HPGe detector (UPu) was a low-energy detector with a 0.15-mm thick beryllium (Be) window and a 15-mm thick crystal. The reduced crystal thickness was used to preferentially detect lower energy photons while allowing higher energy photons to pass through without depositing their energy in the detector.

The coaxial detector was energy calibrated and the gain adjusted using the 661.7 keV ^{137}Cs and the 605 keV ^{134}Cs gamma peaks from the fuel. The planar UPu detector

was calibrated using a low-activity thorium source. (The energy calibration for the UPu detector was improved when the XRF peak analysis was performed.) While taking measurements, the coaxial and UPu detectors were interchanged depending on the desired energy range of the measurement.

Table II. MCA settings taken at ORNL for the October 2011 SNF measurements

	COAX_HI	COAX_LO	UPu
MCA	200974976	97-6361	97-5824
HV	3500 V	None	-1500 V
Coarse Gain	x10	x20	x40
Fine Gain	1.8167x	1.3579x	1.7501x
S-fine Gain	0.999998x	0.999998x	0.9975x
Rise Time	5.6 µs	5.6 µs	5.6 µs
Flat Top	0.9 µs	0.8 µs	0.9 µs
Pole Zero	3659	3669	3300

2.2 October 2011 SNF Measurement Procedure, Data and Results

The following procedure was used for the measurements.

At the ORNL Irradiated Fuels Examination Lab, the ORNL technicians removed the TMI 616B fuel rod from the shipping tube using the pneumatically controlled claws. They placed the fuel rod on the ADEPT system and the length of the fuel rod was measured. The ADEPT system had an offset of approximately 6 mm. This offset was not taken into account for the following measurement positions.

The first task was to find a useable counting position on the 616B rod that was not an inter-pellet space. The count rate from the ^{137}Cs gamma was expected to noticeably decrease at an inter-pellet spacing. Using the coaxial detector, the rod was

"scanned" using the ADEPT system to move the rod in small increments and take counts. The count rate from the 661.7 keV ^{137}Cs peak was measured to determine how it changed with rod position (Table III). Based on the recorded counts along the rod, the center of a pellet was determined to be at position 297 mm. The detector was switched to the UPu and the 297 mm position was counted for approximately 3.3 hours to measure the Pu and U XRF in the low-energy range. The detector was switched back to the coaxial detector and counts were made at the same position for 30 min to measure the Cs peaks and other high-energy gamma radiation from the rod.

Table III. Using the coaxial detector, the ^{137}Cs 661.7 keV count rate was measured along the 616B rod length to determine the center of a fuel pellet

Position (mm)	Count time (sec)	^{137}Cs Peak Counts (counts)	^{137}Cs Peak Count Error (counts)	^{137}Cs Peak Count Rate (counts/sec)	^{137}Cs Peak Count Rate Error (counts/sec)
308	478.11	3.25E+06	1823	6.80E+03	3.813
304	726.96	4.89E+06	2235	6.73E+03	3.074
300	1800	1.22E+07	3535	6.78E+03	1.964
298	251.65	1.70E+06	130	6.76E+03	0.517
297	1800	1.18E+07	3480	6.56E+03	1.933
296	345.25	2.35E+06	1550	6.81E+03	4.490

Next, the rod position was moved to 450 mm using the ADEPT system. The purpose of the next set of measurements was to find the spacer grid within the fuel rod. The spacer grid was expected to be approximately 100 mm wide. To determine its location, the fuel rod would be scanned using the ADEPT system and multiple, short

gamma measurements of the ^{137}Cs peak were taken until a depression in the gamma-ray activity was found. From previous measurements of the 616B rod in January 2009, the rod spacer was expected to be located 400 mm from the rod end. The rod was initially positioned with position 450 mm directly in front of the collimator and detector, and a 1-min count was taken with the coaxial detector. The 1-min count was repeated over the rod length to find the spacer grid (Table IV). Additional 1-min counts were taken on the opposite end of the rod to verify that the grid spacer was not on that side.

Table IV. 1-min counts of the 661.7 keV ^{137}Cs peak were taken using the coaxial detector along the 616B rod length to determine the position of the spacer grid

Position (mm)	^{137}Cs Peak Counts (counts)	^{137}Cs Peak Count Error (counts)
432	3.87E+05	631
435	3.84E+05	627
438	3.80E+05	624
441	3.78E+05	622
444	3.83E+05	626
447	3.81E+05	625
450	3.74E+05	619
453	3.76E+05	620
456	3.82E+05	625
459	3.82E+05	625
470	3.81E+05	624
480	3.84E+05	627
490	3.89E+05	631

Position 447 mm was chosen as the spacer grid location on the 616B fuel rod. The detector was switched to the UPu HPGe detector and an overnight count was taken (Fig. 15). The count stopped after only approximately 3 hours due to an MCA failure. The next morning, the detector was switched back to the coax and a 30-min count for the 447 mm position was taken (Fig. 16).

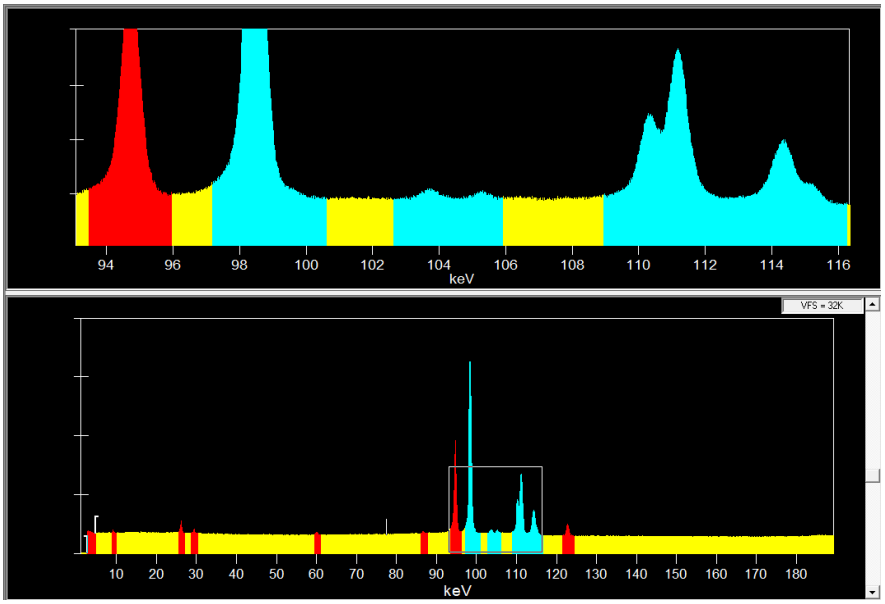

Figure 15. TMI fuel rod 616B UPu 3.6-hour measurement at position 447 mm

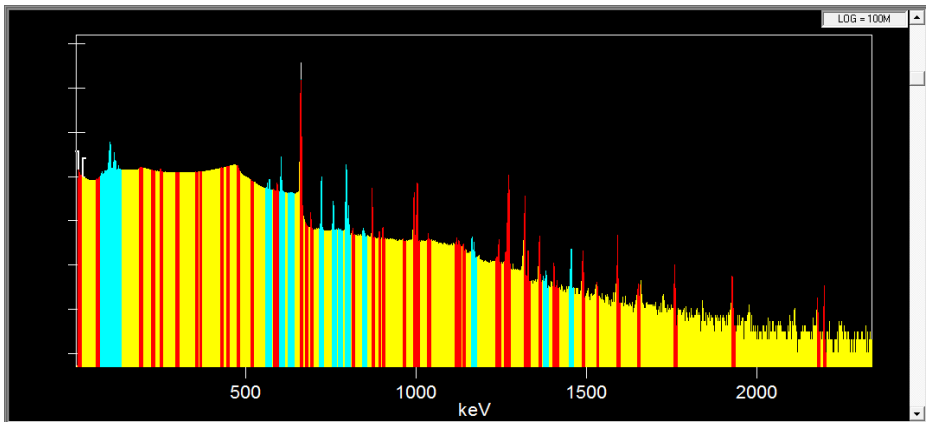

Figure 16. TMI fuel rod 616B coaxial low 30-min measurement at position 447 mm (log plot)

The 616B fuel rod was removed and replaced with the 536C2D fuel rod. The position H6 fuel rod 536C2D was also from TMI but from a different fuel assembly. The fuel rod had an initial enrichment of 4% ^{235}U and a nominal burnup of 49 GWd/MTU. The technicians removed the 536C2D rod from its shipping tube and placed it on the ADEPT system for calibration.

The rod length was measured as 392.21 mm using ADEPT. To determine the fuel pellet spacing, the rod was scanned using the ADEPT system for 1-min counts. Each fuel pellet has a known length of approximately 1 cm. Again, the net ^{137}Cs gamma peak was used to determine the pellet spacing as the detected activity should peak at the center of the fuel pellet (Table V, Fig. 17).

Table V. Using the coaxial detector, 1-min counts of the ^{137}Cs peak in the 536C2D fuel rod were measured in 2-mm intervals to determine the pellet spacings

Position (mm)	^{137}Cs Peak Counts (counts)	^{137}Cs Peak Counts Error (counts)
16	1.48E+03	43
18	1.51E+03	43
20	1.52E+03	43
22	1.48E+03	42
24	4.75E+04	221
26	1.91E+05	433
28	3.33E+05	585
30	3.43E+05	594
32	3.41E+05	592
34	3.51E+05	601
36	3.49E+05	600
38	3.50E+05	600
40	3.44E+05	595
42	3.43E+05	594
44	3.42E+05	593
46	3.49E+05	600
48	3.49E+05	599
50	3.50E+05	600
52	3.43E+05	595
54	3.44E+05	595
56	3.48E+05	599
58	3.49E+05	599
60	3.47E+05	601
62	3.50E+05	598

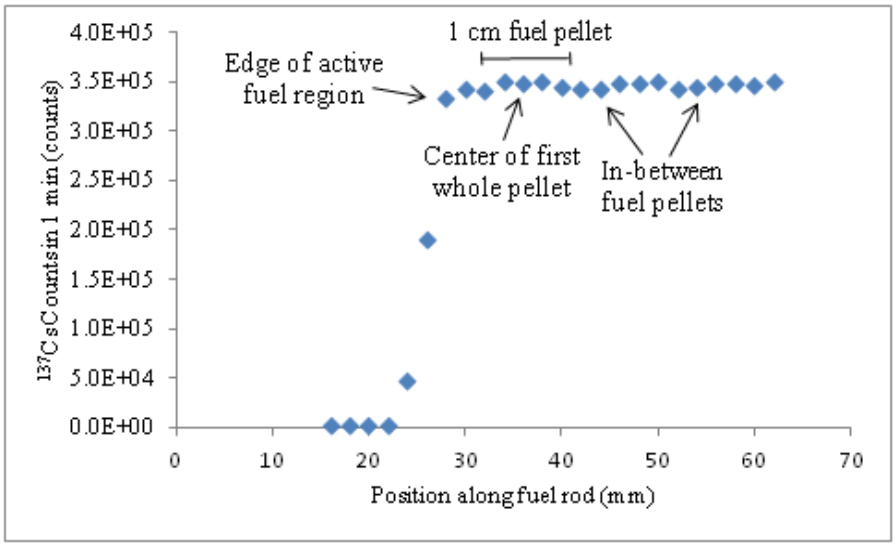

Figure 17. Using the coaxial detector, 1-min counts along the length of the ^{137}Cs activity in the 536C2D fuel rod were taken to determine the individual pellet locations

The center of the first whole fuel pellet on the 536C2D spent fuel rod was identified to be at position 36 mm. A 30-min count was taken with the coax detector at this position (Fig. 18). Then, the detector was switched to the UPu detector and a 3-hour count was taken for the low-energy range to record the Pu and U XRF peaks (Fig. 19).

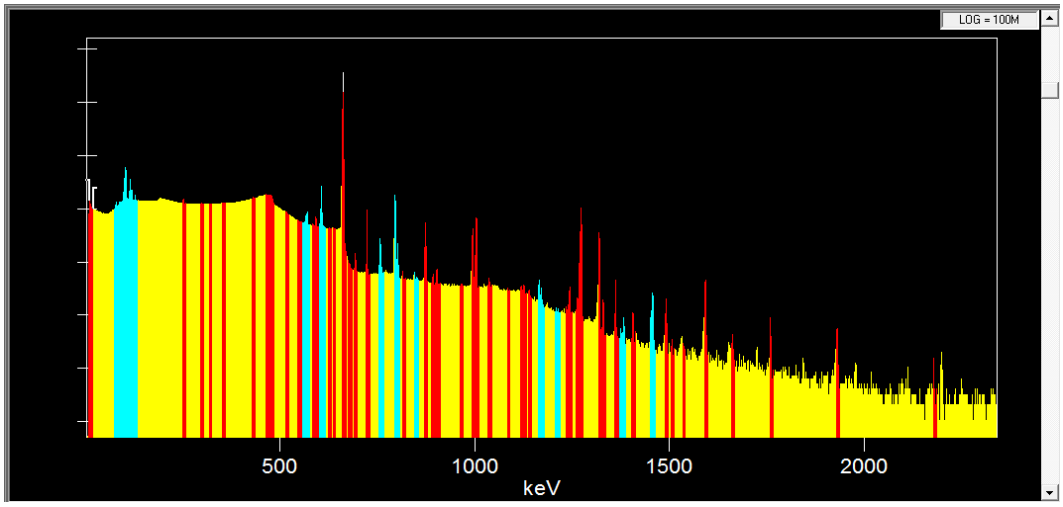

Figure 18. TMI fuel rod 536C2D coaxial low 30-min measurement at position 36 mm (log plot)

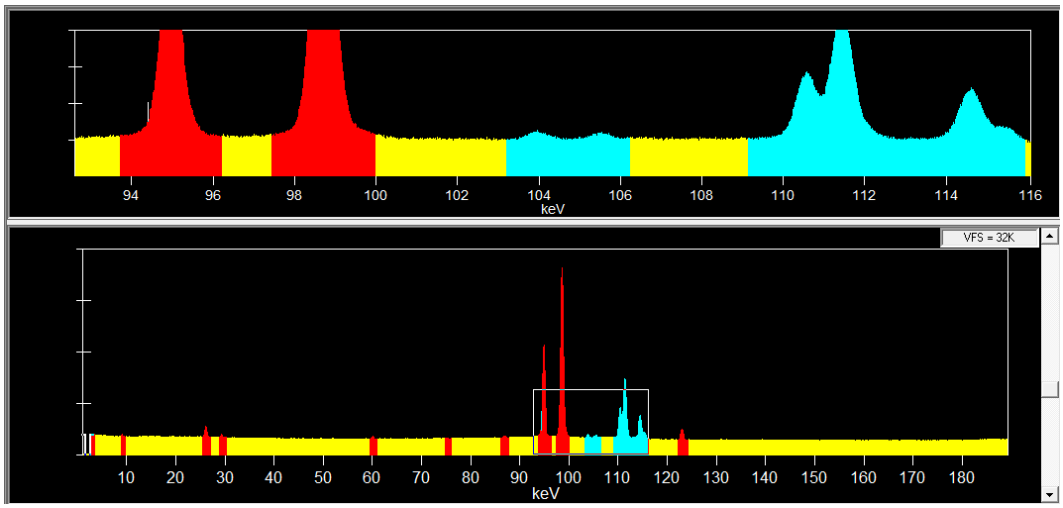

Figure 19. TMI fuel rod 536C2D UPu 3-hour measurement at position 36 mm

The detector was changed back to the coaxial HPGe detector. The next task was to use short counts to determine the spacer grid locations using the ^{137}Cs count rate from the COAX_LO spectra (Table VI, Fig. 20). Based on previous measurements of this

fuel rod, the grid spacer location was expected to stretch from position 269 mm to 380 mm. Over the length of the grid spacer, the ^{137}Cs activity was expected to decrease by 3-4%.

Table VI. Using the coaxial detector, 1-min counts of the ^{137}Cs peak in the 536C2D fuel rod were measured to determine the grid spacer position and the first full pellet location

Position (mm)	^{137}Cs Net Peak Counts (counts)	^{137}Cs Net Peak Counts Error (counts)
270	3.54E+05	603
337	3.42E+05	593
340.3	3.50E+05	600*
342	3.51E+05	600
348	3.37E+05	588
350	2.14E+05	469
352	8.20E+04	290
355	3.43E+05	594
355.69	1.55E+03	43
359.74	1.47E+03	42
363.75	1.52E+03	41
368	1.47E+03	41
372	1.42E+03	40
376	1.44E+03	40
380	1.54E+03	41
382	1.47E+03	41
384	1.47E+03	40
386	1.42E+03	39

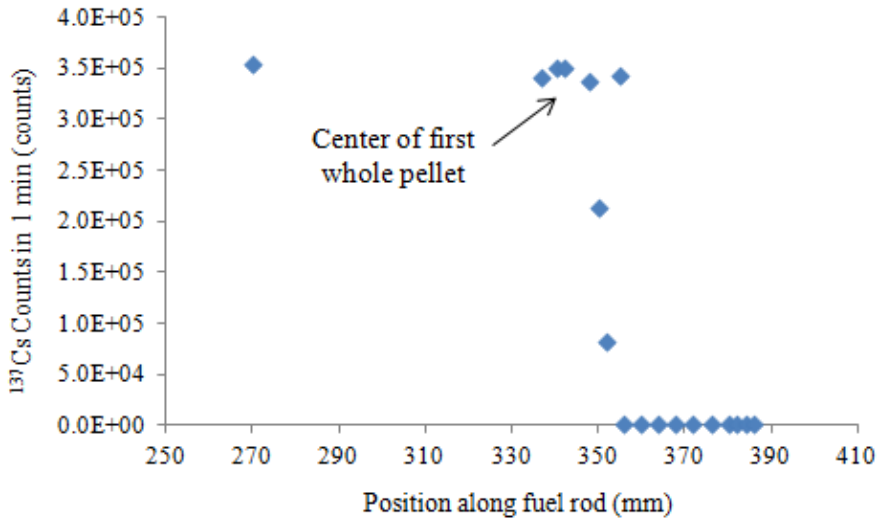

Figure 20. Using the coaxial detector, 1-min counts of the ^{137}Cs peak in the 536C2D fuel rod were measured to determine the grid spacer position and the first full pellet location

Position 342 mm on the 536C2D fuel rod was determined to be the center of the first pellet. The coaxial detector was replaced with the UPu detector and a 13-hour count was taken at this position to record the Pu and U XRF emitted from the fuel (Fig. 21). Once the UPu measurement ended, the detector was switched to the coaxial detector and a 30-min measurement of rod 536C2D at position 342 mm was recorded (Fig. 22). After this measurement, fuel rod 536C2D was reinserted into its shipping tube by the ORNL technicians.

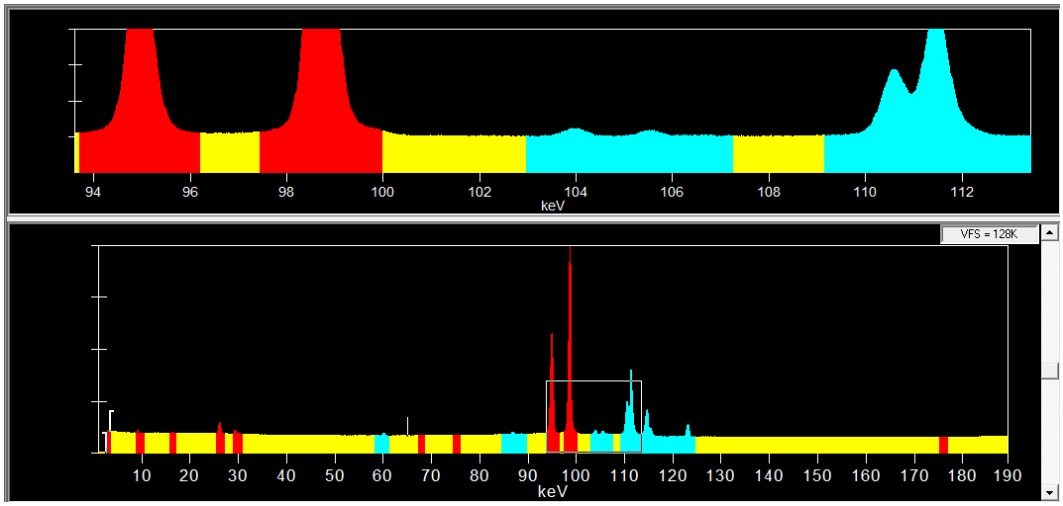

Figure 21. TMI fuel rod 536C2D UPu 13-hour measurement at position 342 mm

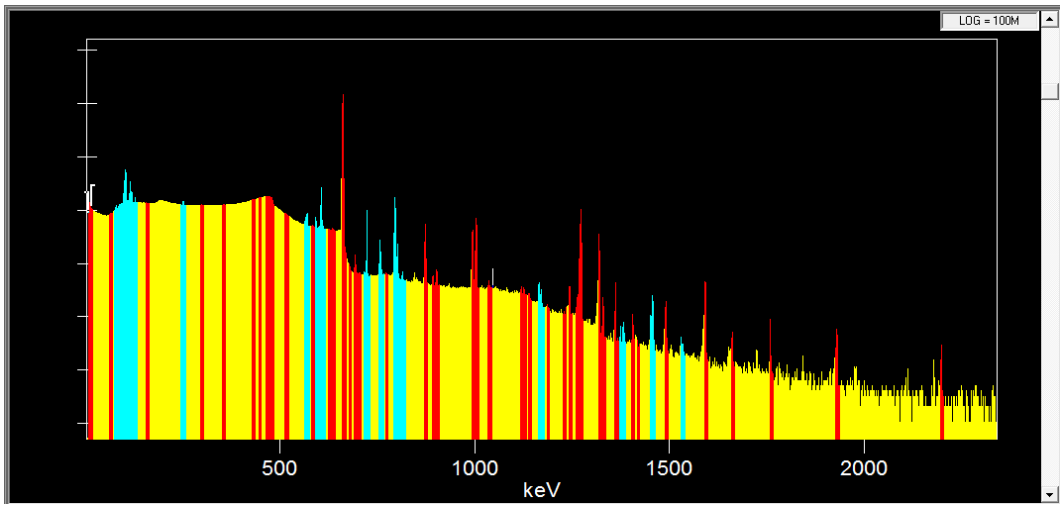

Figure 22. TMI fuel rod 536C2D coaxial low 30-min measurement at position 342 mm

Next, the operators removed fuel rod 616A from its shipping tube and placed it on the ADEPT system. Fuel rod 616A also came from the D5 TMI fuel bundle from NJ05YU with an initial enrichment of 4% ^{235}U. A visual inspection of the rod revealed that rod 616A had a puncture hole on one side. The fuel rod length was calibrated using

the ADEPT system. The 616A rod length was determined to be 744 mm. However, due to the rod imperfection, the ADEPT system had some difficulty grasping the fuel while performing measurement scans. This caused the ADEPT to slip when repositioning the rod which led to inconsistencies in the lateral fuel positioning and the fuel rod length had to be recalibrated several times.

The 616A fuel rod was positioned at 134 mm and a 30-min coaxial detector measurement was recorded (Fig. 23). The detector was switched to the UPu and a 3.5-hour count was taken at the same position (Fig. 24). The rod positioned was then moved to position 230 mm. To obtain a larger energy range, the COAX_HI MCA coarse gain was changed to x5 to increase the energy range to 0-7000 keV. The extended energy range was recorded at position 230 mm for 2 hours using the coax detector (Fig. 25). The coax detector was replaced with the UPu detector and the final measurement taken was at position 230 mm for 18 hours of the low-energy range (Fig. 25).

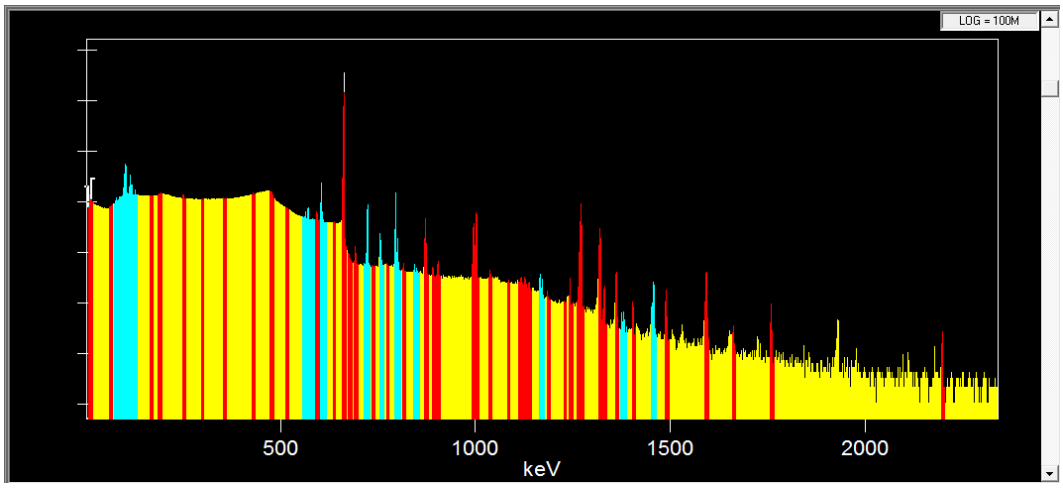

Figure 23. TMI fuel rod 616A coaxial low 30-min measurement at position 134 mm

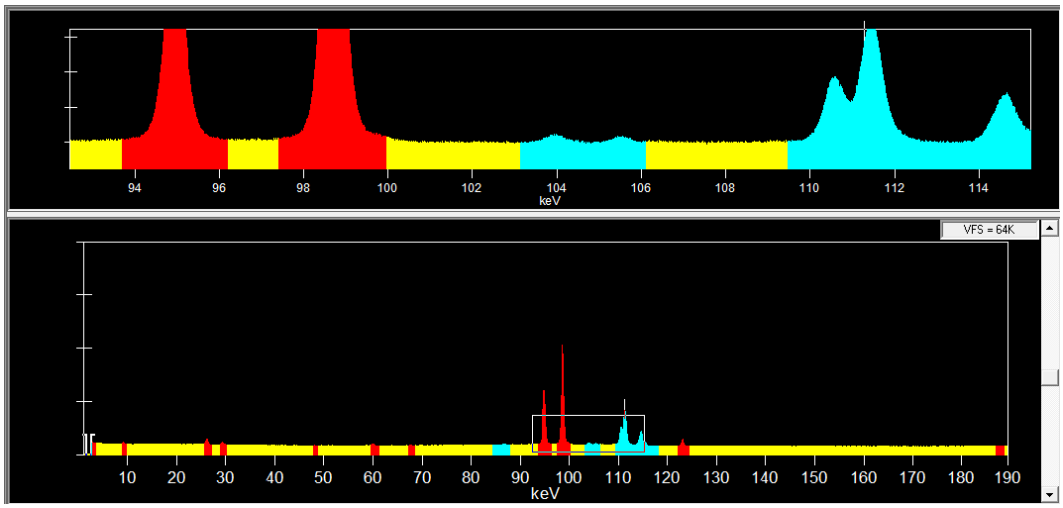

Figure 24. TMI fuel rod 616A UPu 3.5-hour measurement at position 134 mm

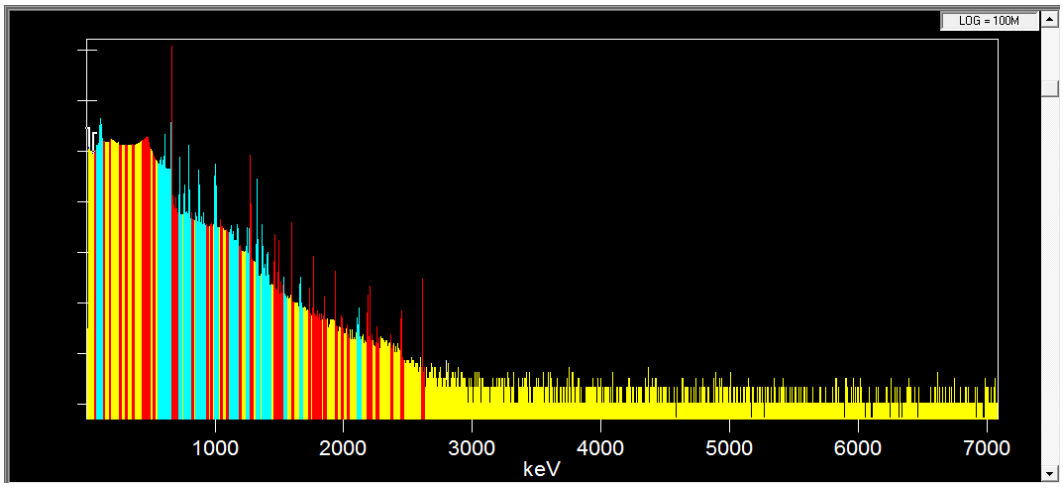

Figure 25. TMI fuel rod 616A coaxial high 2-hour measurement at position 230 mm

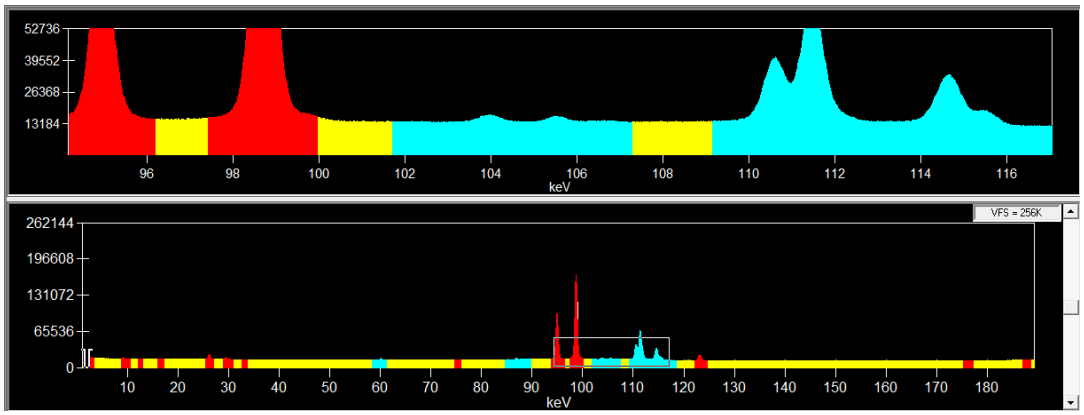

Figure 26. TMI fuel rod 616A UPu 18-hour measurement at position 230 mm

As seen by the presented spectra, a significant amount of Compton background obscured the Pu and U XRF peaks in the 80-125 keV energy range. In the coaxial detector measurements, the Pu and U peaks of interest laid on a huge amount of background radiation caused primarily by the incoherent scattering of the 661.7 keV ^{137}Cs gamma. For the UPu measurements, the detector was specially designed to

preferentially detect low-energy radiation (below 300 keV). However, background radiation in the UPu measurements still reduced the signal-to-noise ratio of the Pu and U XRF peaks and required long count times.

From the four coaxial detector measurements on fuel rods 616B and 616A from the same fuel assembly, the 605 keV ^{134}Cs to 662 keV ^{137}Cs ratios were calculated. The Cs ratio provides information on the fuel burnup and can be correlated to a burnup value by performing irradiation and decay simulations using ORIGEN2, if information about the fuel isotopics and power history are known. Using the four corresponding UPu measurements at the same positions, the 103.7 keV Pu to 95 keV U x-ray peak ratios were calculated (Table VII). The XRF peak ratios were plotted against the corresponding Cs ratios to show the linear correlation between the XRF peaks and the fuel burnup (Fig. 27).

Table VII. The compiled data from the October 2011 TMI spent fuel measurements for fuel rods 616A and 616B

Rod Number	Position (mm)	103.7 keV Pu to 95 keV U X-ray Peak Ratio	605 keV ^{134}Cs to 662 keV ^{137}Cs Peak Ratio
616A	134	0.0357 ± 0.0009	0.0128 ± 0.0001
616A	230	0.0334 ± 0.0004	0.0125 ± 0.0001
616B	297	0.0474 ± 0.0011	0.0143 ± 0.0001
616B	447	0.0404 ± 0.0003	0.0141 ± 0.0001

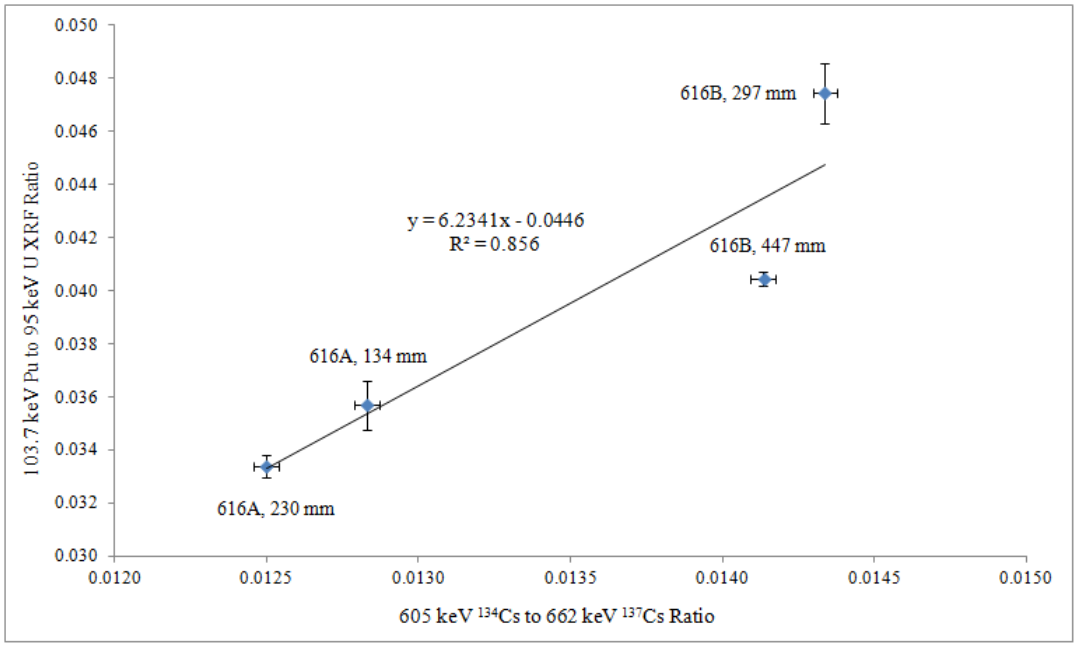

Figure 27. The 616A and 616B TMI spent fuel measurements of the 103.7 keV Pu to 95 keV U x-ray peak ratios versus the 605 keV ^{134}Cs to 662 keV ^{137}Cs ratios

The measurements of rod 616B taken at position 297 mm were included in the plot, however there were some issues with these data. Due to an error with the UPu measurement taken at that position the 3.3-hour measurement could not be properly analyzed in Genie2000. Instead, a much shorter (17-min) measurement was used. This introduced more uncertainty in the Pu and U XRF peaks of interest with errors of 7.4% and 0.9%, respectively. Longer Pu and U measurements (3 hours) had reduced errors of approximately 2.9% and 0.3%, respectively.

The signal-to-noise ratio and percent errors for the 103.7 keV Pu x-ray peak were calculated using Genie2000 for fuel rods 616A, 616B and 536C2D (Table VIII). The count times spanned less than an hour to overnight measurements of 13 and 18 hours.

The signal-to-noise ratio was expected to increase with longer count times while the peak percent error was expected to decrease with longer count times. The percent error followed the expected trend. However, while the very short 616B measurement (0.3 hours) at position 297 mm corresponded to the largest percent error, it unexpectedly had the largest recorded signal-to-noise ratio. Howbeit, this must be weighed against the increased percent error of the peak.

Table VIII. The signal-to-noise ratio and percent error for the 103.7 keV Pu XRF peak calculated using Genie2000 for the six spent fuel rod photon measurements from the UPu detector data

Rod Number	Position (mm)	Count Time (hrs)	103.7 keV Pu X-ray Peak Signal-to-Noise Ratio	103.7 keV Pu X-ray Peak Percent Error
616A	134	4	0.080 ± 0.002	2.52%
616A	230	18	0.071 ± 0.001	1.19%
616B	297	0.3	0.099 ± 0.007	7.38%
616B	447	3.6	0.065 ± 0.002	2.65%
536C2D	36	3	0.073 ± 0.002	2.91%
536C2D	342	13	0.075 ± 0.001	1.24%

For XRF to operate as an efficient and rapid nuclear forensics NDA technique to quantify the bulk Pu content in SNF, the Compton background must be reduced. With a decrease in background radiation, the signal-to-noise ratio of the Pu and U XRF peaks would improve and potentially require a shorter count time to record a significant peak.

2.3 Applicability for Measuring SNF

The proposed method to reduce the Compton background in the HPGe detector is the use of a crystal x-ray spectrometer. Using a crystal of known properties and the Bragg law of diffraction, the Pu and U XRF would be diverted away from the majority of the collimated SNF radiation beam and directed onto a detector. The unwanted radiation would be attenuated by a customized collimator system. The applicability of a flat quartz-crystal x-ray spectrometer for measuring the Pu and U self-induced XRF from SNF is discussed.

2.3.1 Proposed Implementation at Hot Cell Lab or SNF Pool

As stated previously, the proposed flat crystal x-ray spectrometer does not have as many geometrical constraints as the curved crystal spectrometer designs. For the flat crystal to operate, a collimated beam of x rays must pass through the crystal thickness and be diffracted outward conically on the opposite side. This allows for unique applicability for implementation when measuring XRF through hot cell walls or at a SNF pool. Also, for nuclear forensics applications, the detection system should be portable and useable in a variety of situations.

Due to the high radiation levels constantly being emitted from SNF, even after prolonged cooling, measuring XRF and gamma radiation requires heavy shielding. This makes access to the SNF difficult. At the Irradiated Fuels Examination Lab at ORNL, the SNF was always inside of the hot cell with only a very narrow collimated beam directed onto the HPGe detector face (Fig. 28).

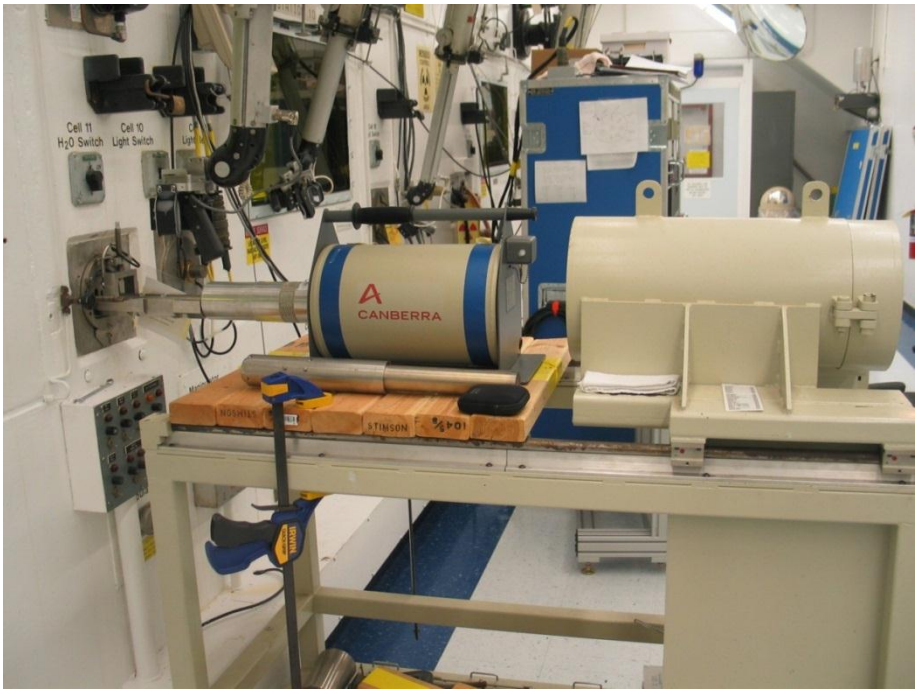

Figure 28. Experimental setup at ORNL with HPGe detector recording spectra from TMI SNF through collimator in hot cell wall

Another potential application for the flat quartz-crystal x-ray spectrometer system would be to measure the spent fuel Pu/U ratio from fuel rods in a spent nuclear fuel pool. After irradiation, spent fuel is taken to a large water pool to provide cooling and allow time for the short-lived, highly radioactive fission products to decay. Similar to hot cells, spent fuel ponds have specially designed ports through which photon spectra can be measured. Spent fuel rods are maneuvered into place directly in front of a pinhole collimator. The only barrier that separates the radioactive pool water from the detection area is a thin aluminum wall. As Al is not particularly dense (2.7 g/cc), it does

not greatly attenuate low-energy x rays. Therefore, Pu and U XRF measurements could be taken using the flat quartz-crystal x-ray spectrometer from SNF in a spent fuel pool.

2.3.2 Design Constraints and Requirements

For the XRF detection method to be a useful nuclear forensics technique, there are certain constraints and requirements which must to be met. An effective nuclear forensics detector should be sturdy, portable and easy to use as the skill level of the future user is unknown. During the ORNL October 2011 SNF measurements, it was clear that the building was not set up for precisely aligned optics experiments. The floors sloped unevenly and there was no equipment available to perform precise measurements. For a crystal spectrometer to be used in such a lab setting, all of the complicated parts of the system need to be calibrated and aligned in a controlled environment. Once the system is properly aligned, it can be brought out into the field. This also implies that the spectrometer and the collimators will need to be fixed in place so that they cannot be inadvertently moved while in the field. Another important feature of a portable piece of instrumentation is sturdiness or at least the ability for it to be fixable in the field. This could mean that it uses standard, replaceable parts and is user friendly.

Some shortcomings of the proposed flat quartz-crystal x-ray spectrometer are that it is a "specific-use" item. The entire system, from the crystal to the collimator to the type of HPGe detector needed, is optimized for a small energy range of radiation, the 103.7 keV Pu and 95 keV U XRF, from a specific source, spent fuel. Also, instead of

simplifying the detection scheme, the use of a crystal spectrometer makes the system more complicated. Conventional gamma spectroscopy simply points a high-resolution gamma spectrometer at a radiation source and takes an energy spectrum measurement. Using a crystal spectrometer system may take a more efficient photon spectrum measurement by reducing the Compton background, but it adds another level of complexity to the analysis.

2.3.3 Benefits of a Flat Crystal Design

The Laue, flat-crystal x-ray spectrometer method is the simplest wavelength-dispersive x-ray detection technique because the crystal remains in a fixed position and orientation during the entire experiment. This is possible for spent fuel rod measurements as the spectrometer system can be optimized for the energy range of interest.

While curved crystal spectrometers require the photon source and detector to be positioned on the tangential Rowland circle, a flat crystal spectrometer does not have this requirement. The flat crystal simply must be positioned in the path of the collimated beam from the SNF and the x rays are diffracted outward conically from the crystal surface according to Bragg's law. Using an HPGe detector, the x rays and gamma rays of interest are recorded while a collimation system blocks the unwanted photons from reaching the detector.

2.4 Additional Components

The quartz crystal does not act as a photon detector. The analyzing crystal acts as the medium through which the radiation passes and is diffracted. The crystal spectrometer system also requires an HPGe detector optimized for low-energy measurements to record the photon spectra. During use, HPGe detectors must be cooled with liquid nitrogen and require a multi-channel analyzer to supply high voltage. To block the unwanted photons from reaching the detector, a customized collimation/shielding system is also necessary. Additionally, the crystal spectrometer system requires a laptop running Genie2000 to record and analyze the spectra.

3. FLAT CRYSTAL DESIGN

The following sections provide details of the design of the flat quartz-crystal x-ray spectrometer system. The spectrometer design was optimized for Pu and U XRF measurements from SNF.

3. 1 Diffraction Mode

As described previously in Section 1, crystal spectrometers can operate in both reflection and transmission mode which describes the way in which the incident x rays are diffracted by the crystal. In reflection mode, the incident x rays reflect off of the surface of the crystal while in transmission mode the x rays pass completely through the crystal and are diffracted on the opposite side. For reflection mode, the crystal reflection planes lie parallel to the crystal surface. However for transmission mode, the diffraction planes lie perpendicular to the crystal surface (Fig. 29)

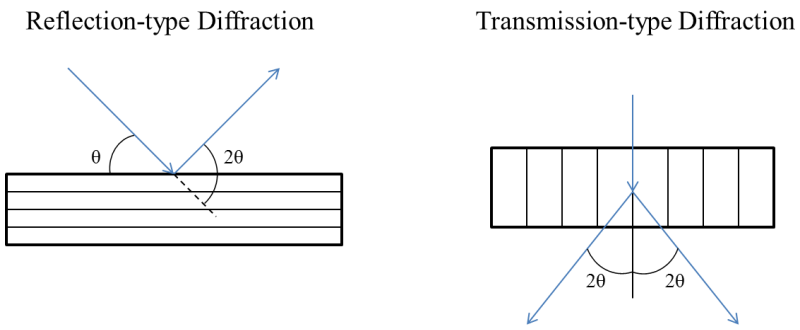

Figure 29. Basic modes of x-ray diffraction by a crystal: reflection and transmission

According to several references, hard x rays, or x rays with energies greater than 10 keV, are better suited for transmission-mode diffraction[15,18,19]. High-energy photons do not interact with matter as readily as low-energy photons. In transmission mode, low-energy x rays would be absorbed by the crystal and greatly reduce diffraction efficiency. Also, in the reflection mode, high-energy x rays would pass through the crystal without being diffracted. In transmission mode, the x rays must travel through a greater crystal length, which increases the probability of coherent scattering and thus diffraction.

The x-ray energies of interest for this research range from 95-120 keV, which are much higher than typical x-ray energies. Therefore, a transmission-type crystal design was selected for measuring the Pu and U characteristics x rays emitted from self-induced XRF in SNF.

3.2 Material and Dimensions

Crystal x-ray spectrometers can be manufactured from a variety of materials, including quartz, silica, calcite, germanium, mica and lithium fluoride[11,15,18,19]. The choice of material depends primarily on the application, crystal structure and cost.

For the early wavelength-dispersive spectroscopy, physicists recorded the physical position of the diffracted spectra. From these films or photographs, they were able to determine properties of the analyzing crystal or the diffracted x rays. For these experiments, a high resolving power was necessary to separate the diffracted beams.

The dispersion efficiency, or angular spread of the diffracted beam, depended primarily on the energy of the incident x ray and the crystal lattice spacing.

The interplanar spacing of a specific crystal depends on the crystal material and how the crystal is cut. Crystals can be cut, or cleaved, along specific crystallographic structural planes. Depending on the angle at which the crystal is cleaved, different lattice structures can be selected. Thus crystal materials, such as quartz or germanium, have multiple possible Miller indices. Also, each Miller index describes a specific interplanar spacing (Table IX).

Table IX. Analyzing crystals composed of a variety of materials have different reflection planes, interplanar spacings and reflection efficiencies[11]

Analyzing Crystals					
Crystal	Reflection Plane	2d Spacing (A)	Lowest Atomic Number Detectable		Reflection Efficiency
			K Series	L Series	
Topaz	(303)	2.712	V (23)	Ce (58)	Average
Lithium Fluoride	(220)	2.848	V (23)	Ce (58)	High
Lithium Fluoride	(200)	4.028	K (19)	In (49)	Intense
Sodium Chloride	(200)	5.639	S (16)	Ru (44)	High
Quartz	(101)	6.686	P (15)	Zr (40)	high
Quartz	(100)	8.5	Si (14)	Rb (37)	Average
Penta erythritol	(002)	8.721	Al (13)	Rb (37)	High
Mica	(002)	19.8	Na (11)	Fe (26)	Average
Lead Stearate	(101)	100	B (5)	Ca (20)	Average

From Bragg's law (Eq. 2), an obvious relationship between the incident x-ray wavelength, crystal interplanar spacing and the diffraction angle exists. The smaller the

interplanar spacing, the larger the resulting diffraction angle for a specific x-ray energy, and vice versa (Table X). Thus to significantly diffract high-energy x rays away from the primary radiation beam, a small interplanar spacing is necessary.

Table X. Energy-dependent photon diffraction angles from a flat quartz-crystal with an interplanar spacing $2d$ = 0.1624 nm

Photon Source	Energy (keV)	λ (nm)	Bragg Angle θ (°)	Diffracted Angle 2θ (°)
U (XRF)	94.7	0.01306	4.613	9.225
U (XRF)	98.4	0.01266	4.471	8.942
Pu (XRF)	103.7	0.01196	4.223	8.447
Eu-155 (γ)	105	0.01182	4.174	8.348
U (XRF)	110	0.01128	3.983	7.966
U (XRF)	111	0.01118	3.947	7.895
U (XRF)	114	0.01088	3.841	7.683
Eu-154 (γ)	123	0.01009	3.562	7.124
Ce-144 (γ)	133	0.00933	3.293	6.587

The crystal dimensions were limited by what could be commercially manufactured and by the experimental conditions. Due to the initial collimation through the hot cell wall, there was no need to create a crystal much larger than the collimated beam.

For transmission-type crystal spectrometers, the crystal thickness is an incredibly important parameter. Depending on the x-ray energies being analyzed, a crystal thickness which optimizes diffraction while minimizing absorption and incoherent scattering must be selected. A complicated relationship between the x-ray energies of

interest, crystal material, electron density and lattice structure defines the most useful crystal thickness.

In addition, the thickness of the crystal (*e*) and the size of the collimated primary beam source (*2r*) affect the size, or Laue spot, of the diffracted beam on the detector (Fig. 30). The thicker the crystal or the greater the initial source width, the larger the recorded Laue spot.

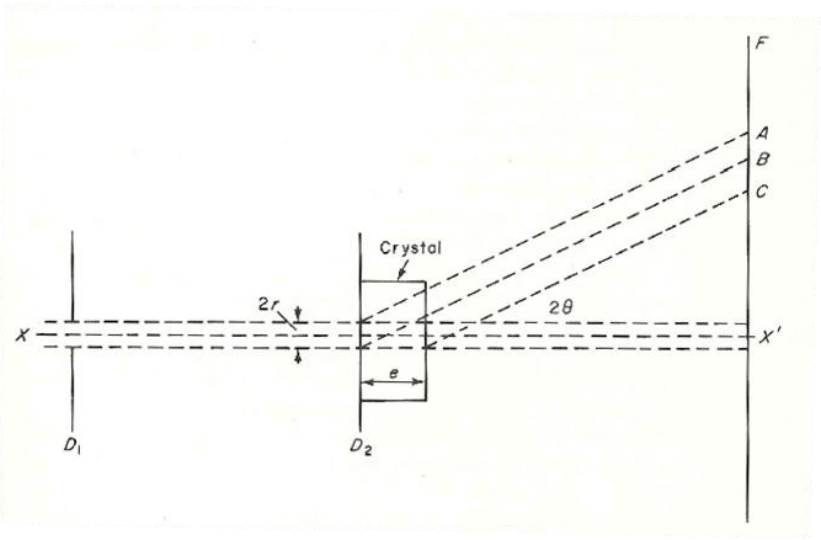

Figure 30. The Laue spot sizes are a function of the crystal thickness (*e*) and the width of the incident x-ray beam (*2r*) [11]

Through an extensive literature search, a crystal thickness of 0.25 mm was selected. This thickness was chosen specifically to optimize diffraction of the 80-125 keV photons from the SNF.

The cost of the desired crystal is another important component when purchasing an analyzing crystal. Specialized manufacturing of a desired crystal material with a specific lattice structure and customized dimensions increases the price. Also, some analyzing crystal materials, such as germanium, are expensive without the additional manufacturing costs. Germanium is used as a semiconductor detector and the cost of a single crystal can exceed several thousand dollars[20]. Quartz is a practical analyzing crystal material and is commonly used in crystal x-ray spectrometer experiments[18,19]. Quartz can be produced with very few imperfections and is available at much lower costs.

3.3 Diffraction Efficiency

The diffraction process is the coherent scattering of x rays by individual atoms making up the crystal structure. The scattering power, or probability that an individual x ray will be scattered, is a function of the orbital electron density of the atom, the angle of diffraction and the energy of the primary x rays[21]. The scattering of the x-ray beam increases with proton number such that heavy nuclei scatter x rays more strongly[10]. The intensity of the diffracted rays, or the probability of coherent scattering, depends on the scattering power and the phase differences between the scattered waves. The phase difference depends on the crystal structure and the orientation of the lattice planes. Thus the diffraction efficiency of a specific crystal depends on the complicated relationship between the crystal material, orientation and structure of the lattice planes, and the wavelength of the x rays[21].

Crystal spectrometers have relatively low diffraction efficiencies of 20-50%[21]. From a literature review, the expected diffraction efficiency of the proposed flat quartz crystal is within the stated range. While the efficiency is an important parameter of the spectrometer, it is balanced with the ability of the system to block high-energy gamma rays from reaching the detector. With a decreased Compton background, even if fewer Pu and U x rays reach the detector their effective worth will be greater. With lower background, the signal-to-noise ratio will increase and the percent error of the peaks will decrease.

3.4 Resolution

The resolution of the diffracted x-ray beam depends on the crystal structure. Beam resolution is very important for curved crystal spectrometers as it relates to the focusing capabilities of the system. For flat crystals the resolution is dependent on the initial collimated source width. The broader the source, the wider the diffracted beam spots appear on the detector face. Generally flat crystal resolution is very high such that individual x-ray energies can be easily resolved on a photographic plate, if desired.

From a compilation of all of these factors, a flat-quartz crystal was selected. Quartz was chosen as the crystal material as numerous successful x-ray spectrometer experiments used quartz[15,18]. The flat crystal will be used in transmission mode such that as x rays pass through the crystal and are diffracted on the opposite side they will diverge outward conically. This requires additional collimation, which will be discussed in the next section. The dimensions of the analyzing crystal were chosen based upon the

experimental conditions determined from the ORNL measurements. As the hot cell wall collimator had a 0.3 cm diameter, the crystal was sized proportional to this dimension.

The final analyzing crystal dimensions selected were 3 cm tall by 4 cm wide by 0.25 mm thick (Fig. 31). The lattice structure of the selected quartz crystal was (404) with an interplanar spacing (2d) of 0.1624 nm. The expected angles of diffraction for the 103.7 keV Pu x ray and the 95 keV U x ray were 8.447° and 9.225°, respectively. While this did not represent a large angular displacement from the transmitted beam, a customized collimator which allowed the desired diffracted photons to reach the detector while blocking the unwanted radiation was designed.

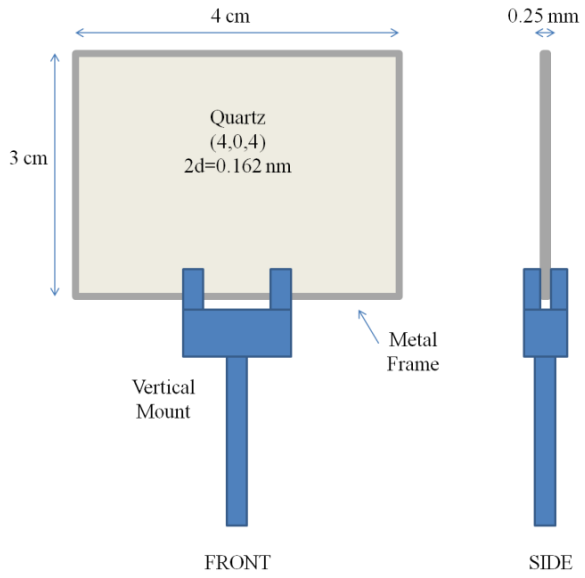

Figure 31. The dimensions and material information for the proposed flat quartz analyzing crystal for an x-ray spectrometer system

4. COLLIMATION SYSTEM DESIGN

The following section describes the customized collimation system that was designed specifically for the transmission-type flat quartz-crystal x-ray spectrometer for the detection of Pu and U x rays.

4.1 Shape and Dimensions

The shape and dimensions of the collimator were influenced by the experimental conditions at the ORNL hot cell lab and by the expected diffraction angles of the Pu and U x rays through the quartz crystal (Fig. 32).

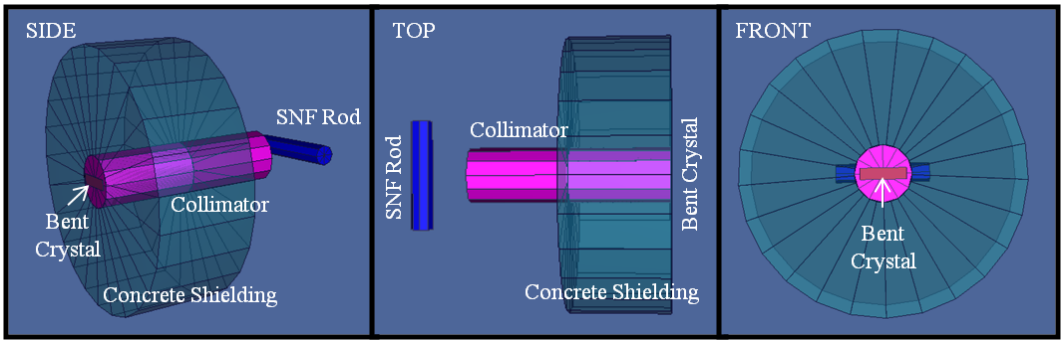

Figure 32. A 3D view of the spent fuel measurement system, including the SNF rod, the primary pinhole collimator, the hot cell wall concrete shielding and the quartz crystal

A customized collimation system was devised. The primary collimator acted as a pinhole collimator through the hot cell wall to allow SNF photon measurements. The primary collimator was used to collimate the photons incident on the diffracting crystal.

The width of the primary collimator was defined by the ORNL hot cell lab collimator. For the spent fuel measurements performed at ORNL in October 2011, the length and width of the primary collimator was 167 cm and 0.3 cm, respectively. Therefore, the divergence of the collimated photon beam from the spent fuel was 0.21°. Also, the primary collimator ensured that the photon beam hitting the diffracting crystal originated from only locations on the spent fuel rod. The collimator would be placed directly in front of the flat crystal. Thus the x rays would be diffracted to some known Bragg angle and be traveling forward, spreading outward conically (Fig. 33). The purpose of the collimator was to allow only x rays with energies in the range of interest (80-125 keV) to arrive unattenuated at the detector.

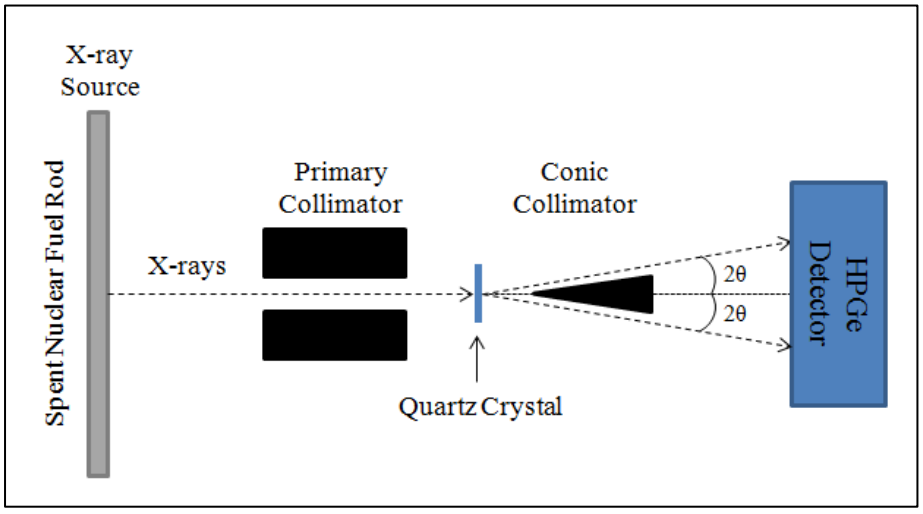

Figure 33. Side view of the entire crystal spectrometer system, including the SNF x-ray source, the initial pinhole collimator, the flat analyzing crystal, the secondary conic collimator and the HPGe detector (not to scale)

Since to the diffracted x rays would be traveling outward conically from the analyzing crystal surface, the customized secondary collimator must be conic in shape. From Bragg's law of diffraction, the higher the x-ray energy then the smaller the diffraction angle and vice versa (Fig. 34). Thus, after passing through the crystal, the higher-energy diffracted x ray paths would be deflected only slightly from the transmitted beam path while the lower energy diffracted x rays would have larger diffraction angles.

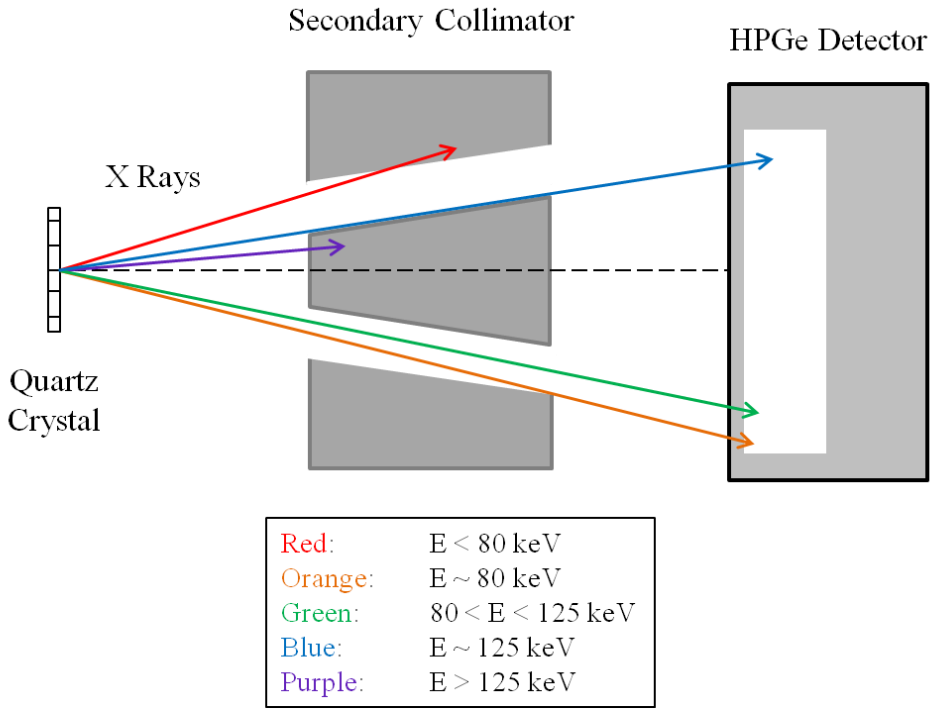

Figure 34. The diffraction angles over the range of desired x-ray energies by a flat crystal onto an HPGe detector (side view)

When selecting the dimensions of the conic collimation system, certain requirements must be met. First, the size of the conic collimator must be realistically applicable for use in a portable detector. The angle of the cone shape was selected such that the highest desired energy photon (~125 keV) could successfully traverse the collimator and reach the detector without running into the inner cone. Also, because of the fixed angle and conic shape, as the cone length increased, so did the diameter of the cone base. Since the collimator must be inserted between the quartz crystal and the detector, the base of the cone could not completely obscure the effective HPGe detector face. If the cone base was too wide, it would completely block all photons, even diffracted x rays in the energy range of interest, from reaching the detector crystal.

After searching through the available low-energy HPGe (LEGe) detectors offered by manufacturing companies, a semiconductor detector with a germanium crystal detection area of 2000 mm^2 (25.23 mm radius) was found. The Canberra GL2015R LEGe semiconductor detector has a 0.5-mm thick Be window and a 15-mm thick germanium crystal[22]. The thin Be window does not greatly attenuate low-energy photons and the narrow Ge crystal preferentially absorbs low-energy radiation. The conic collimator dimensions were based on this commercially available detector and the properties of the analyzing crystal described in Section 3.

An outer collimator was added to the system to block scattered photons and lower-energy x rays from reaching the HPGe detector. The outer collimator encased the inner conic collimator, leaving a narrow, angled air gap in between (Fig. 35). Only in this narrow, air-filled region could the diffracted x-ray energies of interest pass through

the collimator and reach the HPGe detector. As a simplification in the MCNP simulation, the inner collimator of the secondary collimator was not attached to the outer shielding. In reality, small Al bars would hold the inner cone inside the outer collimator.

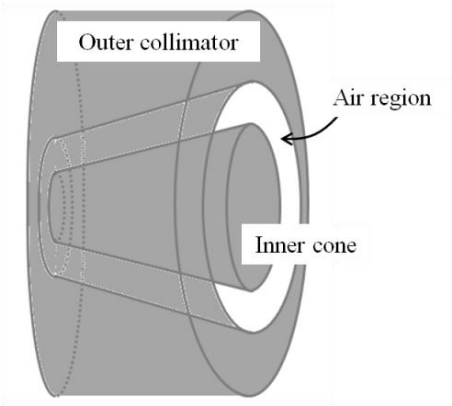

Figure 35. A 3D view of the secondary conic collimator and outer shielding

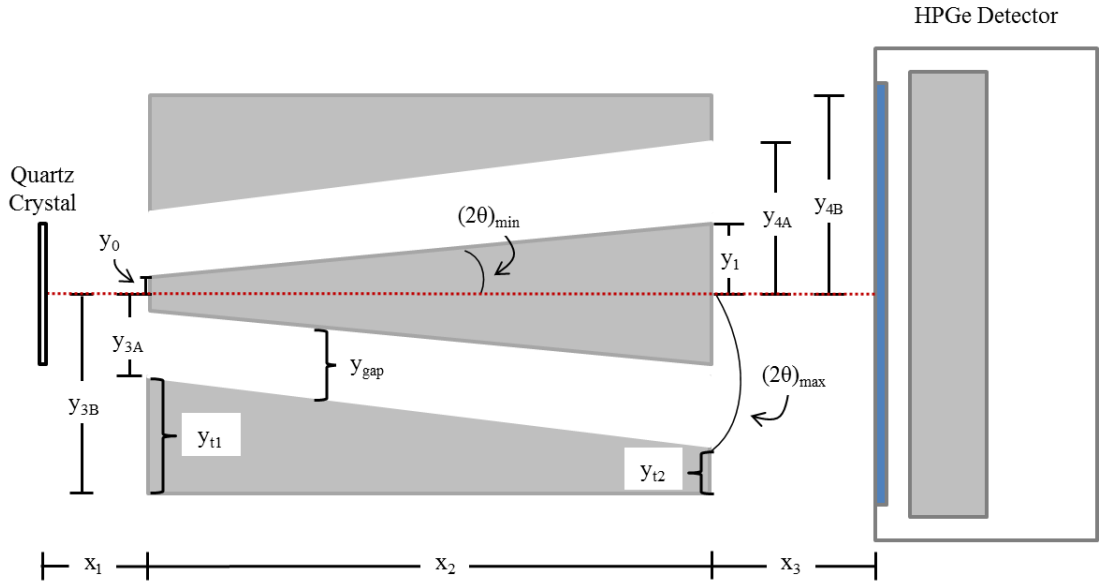

Figure 36. The physical parameters of the analyzing crystal and the HPGe detector were used to determine the conic collimator system dimensions (not to scale)

Figure 36 shows the parameters that were selected to allow only diffracted x rays in the energy range of interest to successfully traverse the conic collimation system. The distance from the analyzing crystal to the conic collimator (x_1) was determined by setting the inner cone lower base radius (y_0) at 0.25 cm:

$$x_1 = {}^{y_0}/_{\tan 2\theta_{min}} = {}^{0.25cm}/_{\tan(6.95°)} = 2.05 \text{ cm} \quad (4)$$

where the highest desired energy (125 keV) x-ray wavelength defined the diffraction angle ($2\theta_{min}$) as 6.95°.

The collimator length (x_2) was varied when optimizing the design. Lengths of 8 cm, 6 cm, 4 cm and 2 cm were simulated and compared to quantify how well the unwanted radiation was blocked from reaching the detector. The 8-cm length was used to determine the following collimator dimensions.

The inner cone upper base (y_1) was calculated using $2\theta_{min}$, x_1 and x_2:

$$y_1 = (x_1 + x_2)\tan 2\theta_{min} = (2.05 \text{ cm} + 8 \text{ cm})\tan(6.95°) = 1.23 \text{ cm}. \quad (5)$$

The distance from the end of the conic collimator to the HPGe detector face (x_3) was set to 0.2 cm to replicate the experimental set up at the ORNL hot cell lab. On the opposite end of the collimator near the detector, the distance from the center of the inner conic collimator to the beginning of the outer shielding (y_{4A}) was calculated using the maximum allowed diffraction angle ($2\theta_{max}$) of 10.96° for the lowest desired energy photon (80 keV) and the lengths x_1 and x_2:

$$y_{4A} = (x_1 + x_2)\tan 2\theta_{max} = (2.05 \text{ cm} + 8 \text{ cm})\tan(10.96°) = 1.75 \text{ cm}. \quad (6)$$

The air gap between the inner conic collimator and the outer shielding (y_{gap}) was held constant at 0.5 cm as this allowed x rays in the energy range of interest to

successfully traverse the collimation system. The initial thickness (y_{t1}) of the outer shielding was set at 2 cm. Based on the geometry of the system, this set the final thickness (y_{t2}) as approximately 1 cm. The length from the center of the inner conic collimator to the beginning of the outer shielding (y_{3A}) was calculated using y_0 and y_{gap}:

$$y_{3A} = y_0 + y_{gap} = 0.25 \text{ cm} + 0.5 \text{ cm} = 0.75 \text{ cm}. \quad (7)$$

The full radial height of the outer shielding (y_{3B}, y_{4B}) was determined by summing y_1, and y_{gap} and y_{t1}:

$$y_{3B} = y_1 + y_{gap} + y_{t1} = 0.25 \text{ cm} + 0.5 \text{ cm} + 2 \text{ cm} = 2.75 \text{ cm}. \quad (8)$$

The initial (y_{3B}) and the final (y_{4B}) outer-shielding dimensions were equal:

$$y_{4B} = y_{3B} = 2.75 \text{ cm}. \quad (9)$$

Figure 37 shows a summary of the dimensions for the 8-cm long conic collimation system. A table of the 6-cm, 4-cm and 2-cm long conic collimation system dimensions appears in Appendix A.

When the customized conic collimator prototype is fabricated, all of the components, including the primary pinhole collimator, secondary conic collimation system and flat crystal, will be combined into a single element. This single collimator will secure onto the end of the UPu detector when taking SNF measurements. This will ensure that the individual components are properly position and remain fixed throughout the experiment.

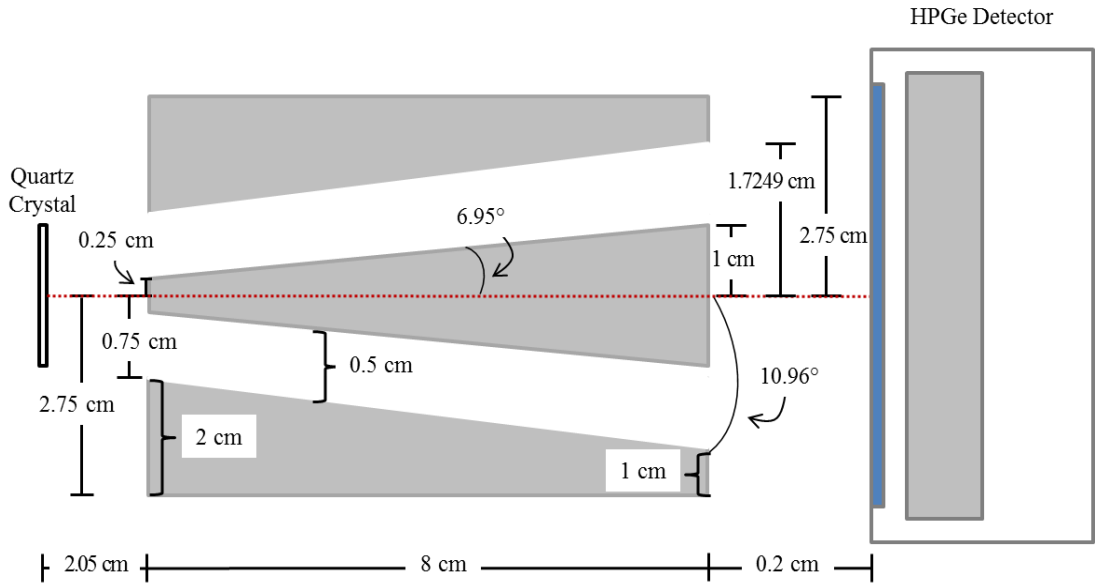

Figure 37. Cross sectional view of the overall conic collimator system including dimensions (not to scale)

Another option was to use a Soller collimator, a multi-channel narrow slit collimator. The Soller slits are commonly used in crystal x-ray spectrometer systems, such as DuMond schemes[15,19]. In the DuMond method, after the x rays pass through the curved crystal and are diffracted, they diverge[15]. Using an angled, multi-channel slit collimator, DuMond was able to isolate a narrow energy range to record only the desired x ray. All other photons, which were not diffracted to the angles allowed by the Soller slits, were attenuated. However, for the purpose of measuring a wider energy range (80-125 keV), the Soller slits were not applicable. The multi-channel collimator would have greatly reduced the efficiency of the spectrometer system by blocking many of the diffracted photons.

4.2 Material

Once the dimensions were determined, a suitable material for the collimator/shield had to be selected. Three collimator materials were considered: tungsten, lead and stainless steel. Each material had advantages and disadvantages. For any of the proposed materials, the collimator would be professionally machined to the desired dimensions.

Due to its high density (19.25 g/cc), tungsten (W) was expected to be the most effective at blocking the unwanted photons from reaching the detector. Tungsten is a strong, dense metal which can maintain its structure for many years. One disadvantage of tungsten is its high cost.

Lead (Pb) has a lower density (11.34 g/cc) but is a common and less expensive radiation shielding material. However, Pb has several drawbacks. Machining Pb can be difficult due to health concerns as it is toxic. Handling of Pb should be limited and hands thoroughly cleansed after direct contact. One advantage of lead is that it is highly malleable and easy to shape. However, this can be a negative factor when designing a precise collimation system. Over time, lead collimators can lose their shape and begin to slump under their own weight. Since the collimator design was customized to allow only a certain Bragg angle of diffracted x rays to traverse the conic collimator without attenuation, the collimator must be able to hold its structure or it will block the x rays of interest. Lead also emits 75-85 keV x rays when excited by high-energy gammas. These x rays can be attenuated by surrounding the Pb with aluminum. The Al could also act as a safety barrier when the collimator was being handled.

Stainless steel is the least dense (8.03 g/cc) proposed collimator material. It is also the least expensive option but was expected to be the least effective shield. Stainless steel is also easy to machine. Stainless steel is composed of iron, carbon, chromium, nickel, phosphorous, manganese and sulfur.

A quantitative comparison of the ability of the three collimator materials to block unwanted photons is presented in Section 5.

5. X-RAY SPECTROMETER SIMULATIONS

The following sections describe the simulations performed using the computer code MCNP to model the detection capabilities of the crystal spectrometer system. Two x-ray source definitions were modeled in MCNP to quantify the ability of the x-ray spectrometer to reduce the overall Compton background recorded by the HPGe detector and to improve the signal-to-noise ratio of the Pu and U XRF peaks of interest.

5.1 Spent Fuel Simulation

Alissa Stafford created comprehensive models of the TMI spent fuel for her master's thesis[1]. Initially she modeled the TMI power history in TransLat and decay in ORIGEN2[1,6,23]. She took that source information and used MCNP to model the radiation transport from the spent fuel to an HPGe detector[1,24]. The fuel regions were simulated separately to accurately reflect the radial fuel isotopic differences (Fig. 38)[1]. Her spent fuel simulations were used as the initial source definition in the crystal spectrometer simulations[1].

5.1.1 Geometry and Source Definition

The MCNP model developed by Stafford transported the radiation from the spent fuel onto multiple counts versus energy tally surfaces to measure the incident radiation and to quantify the Compton background contributions from the different system components[1]. She found that the Compton continuum contributions came from the fuel

rod, the shipping tube, the cladding, the detector can and the collimator end[1]. For these simulations, the shipping tube was removed to reflect the actual ORNL experiment.

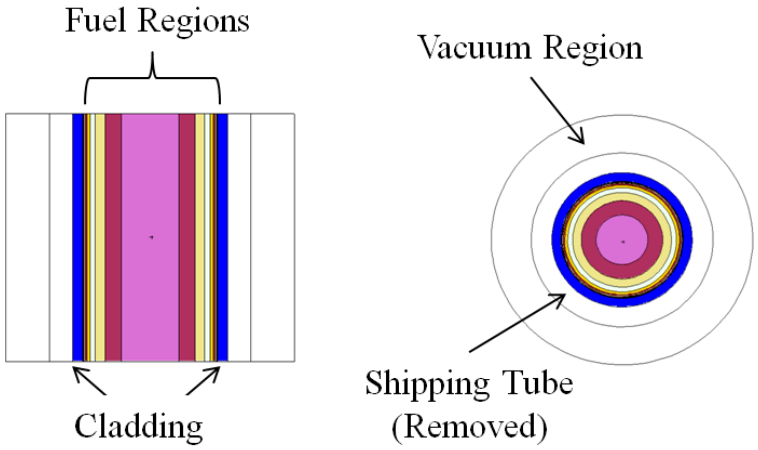

Figure 38. Stafford's TMI MCNP source definition simulation geometry[1]. Left: cross sectional view of fuel length, Right: cross sectional view of fuel

For this research, her MCNP model of the TMI spent fuel was used to take a surface flux (F2) tally of the radiation emitted from the spent fuel[1]. The output from the F2 tally was the energy of the particle coupled to the probability of a count per original number of source particles run in the simulation. This output tally information was scaled to match the experimental system.

The MCNP spent fuel output tally values were normalized to the experimental October 2011 ORNL spent fuel measurements. This offered the most realistic interpretation of the MCNP results as the simulation took into account real fuel measurements, count times, and the exact experimental geometry.

A linear scaling factor was used to normalize the MCNP output values to the spent fuel measurements. The normalization factor (*N*) used was the ratio of the gross peak area from the TMI spent fuel measurements to the MCNP output tally gross peak area for the 95 keV U peak:

$$N = \left({}^{TMI\ Fuel\ Gross\ Counts}/_{MCNP\ Gross\ Counts} \right)\Big|_{95\ keV\ U\ Peak} . \quad (10)$$

The gross counts values were obtained by analyzing the experimental TMI measurements and the simulated MCNP output tally data in Genie2000. The normalization factor scaled the MCNP output tally to a measurement from a planar HPGe detector. The data were examined furthered using the Interactive Peak Fit software in Genie2000.

For a 3-hour count time, the normalization factor between the TMI counts and the MCNP simulation without the secondary conic collimator was found to be 1.68 ± 0.10. The scaling factor was based upon a simulation with the secondary conic collimator removed to more closely replicate the experimentally obtained data.

The F8 tally output from the simulations with the standard spent fuel source (undiffracted) and with the secondary collimator removed were scaled to the ORNL TMI measurements for counts times of 30 min, 3 hours and 6 hours (Fig. 39).

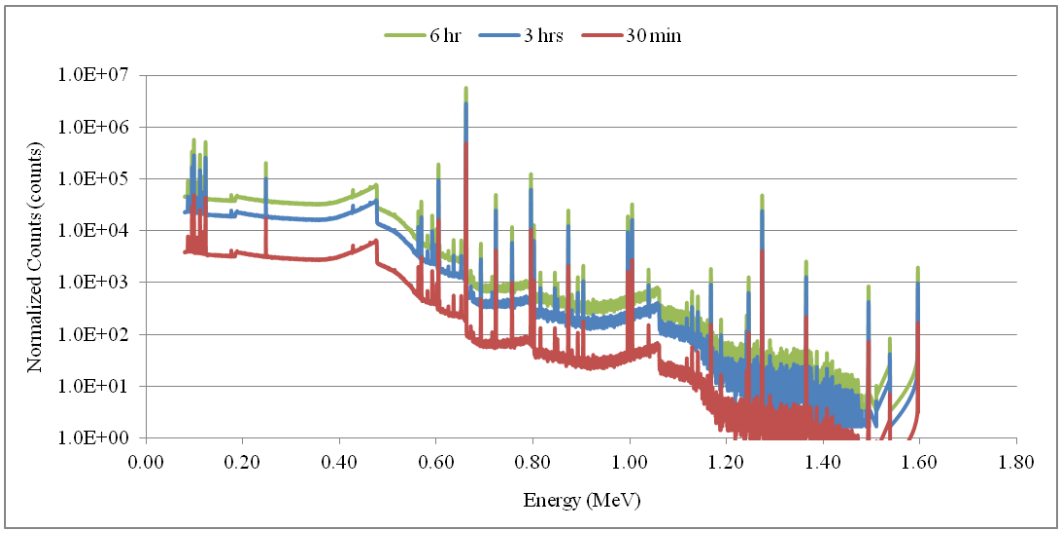

Figure 39. The simulated undiffracted and uncollimated F8 tally output scaled to the ORNL TMI measurements for count times of 30 min, 3 hours and 6 hours

The crystal x-ray spectrometer simulations were separated into two MCNP simulations. The results from Stafford's original simulation were used as the primary radiation source incident on the quartz crystal surface. The second simulation was for the flat quartz-crystal x-ray spectrometer system (Fig. 40).

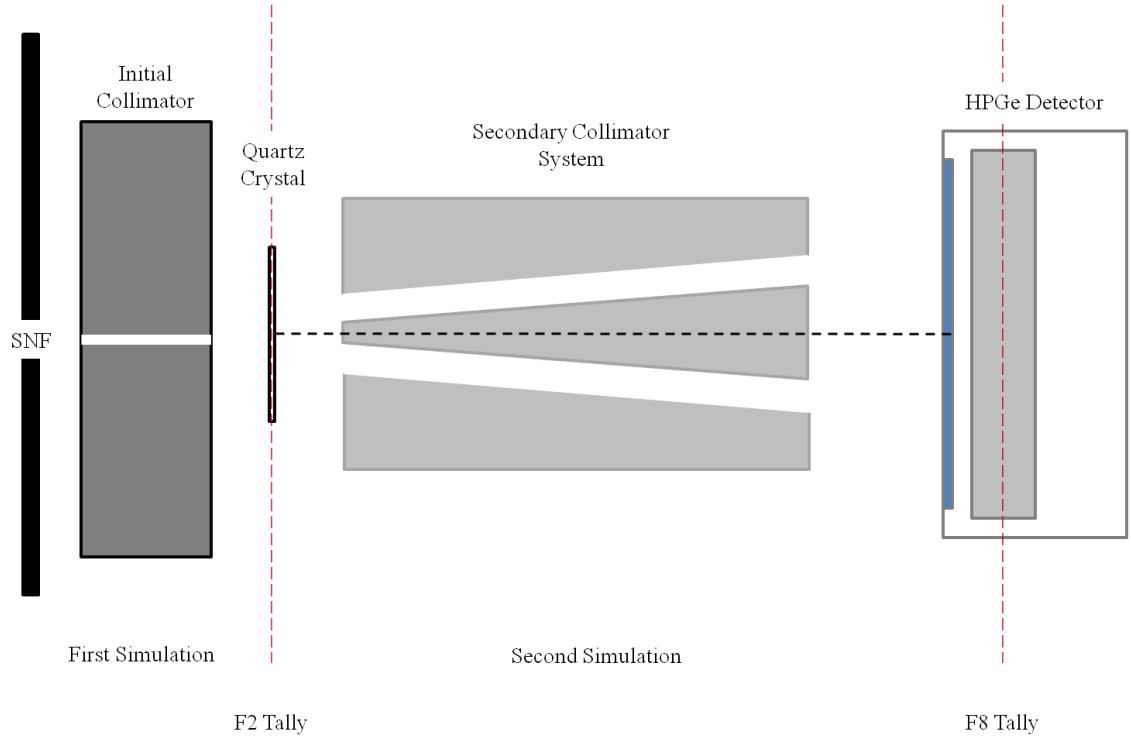

Figure 40. Two MCNP simulations were performed to simulate the SNF incident on the analyzing quartz crystal being diffracted through the conic collimation system onto the HPGe detector (not to scale)

The secondary simulation used the output tally data from the primary simulation as the photon source. When the photons from the initial simulation "hit" the quartz crystal, they were diffracted according to Bragg's Law (Eq. 2). All photons created in the Stafford simulation from 0-1.6 MeV were included in the secondary source definition. However, the MCNP code was unable to simulate the wave properties of light, such as x-ray diffraction. An external routine was devised to simulate diffraction using an energy-direction coupled source definition. To create the energy-direction coupled source definition, the F2 output tally results from the first simulation over the 0-

1.6 MeV energy range were entered into a spreadsheet. Then using the previously noted crystal parameters ($2d$ = 0.1624 nm) and Bragg's law of diffraction (Eq. 2), the Bragg angle for each energy bin was calculated. To communicate the individual photon energy diffraction angles in MCNP, an additional command in the MCNP source definition was used. Basically, the direction of the diffracted photon was linked to the photon energy. For MCNP to correctly interpret these "diffraction angles," an energy function controlling the initial angle of the photons (DIR FERG) command was used. The DIR FERG function read the cosine of the diffraction angle (μ) relative to a line normal to the crystal surface. The command provided a way for MCNP to simulate x-ray diffraction through the quartz crystal. The MCNP deck used to simulate the x-ray diffraction through the collimator onto the HPGe detector is located in Appendix B.

The output from the second simulation (using the energy-direction coupled source) was analyzed to determine the improved signal-to-noise ratio and decreased percent error for the crystal x-ray spectrometer system results.

5.1.2 Simulation Analysis

The flat, transmission-type crystal diffracts the incident x rays outward conically. This was replicated in MCNP by using a card which defined the photon direction according to its energy. Multiple collimator materials and lengths were simulated. The materials W, Pb and stainless steel were simulated and the results compared. Simulations for collimator lengths of 8 cm, 6 cm, 4 cm and 2 cm were compared to runs

with no conic collimator to quantify the reduction in background due to the conic collimator.

The first MCNP calculation did not include the secondary conic collimator. The results from this simulation were used to compare the effect the conic collimator had on reducing the Compton background and preventing unwanted photon energies from reaching the detector. The MCNP output tallies were normalized to the ORNL spent fuel measurements.

Each of the conic collimator materials was simulated in MCNP with the full TMI spent fuel source definition (Fig. 41). The source definition included energy-direction coupling to simulate diffraction by the quartz crystal. The MCNP spectra for the tungsten, lead and stainless steel collimators are shown in Figures 42-44. The 0-1.6 MeV energy range and the 80-125 keV energy range of interest were plotted to determine the effect of the conic collimator on reducing background radiation from reaching the HPGe detector.

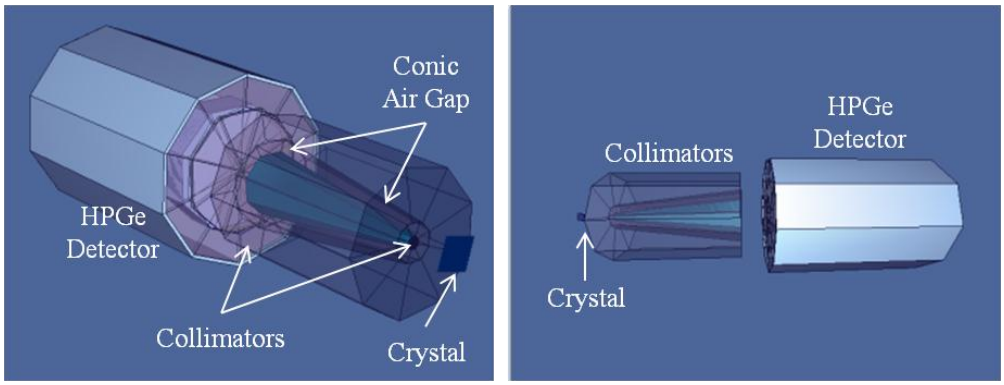

Figure 41. The secondary MCNP simulation with the energy-direction coupled diffraction source incident on the conic collimation system

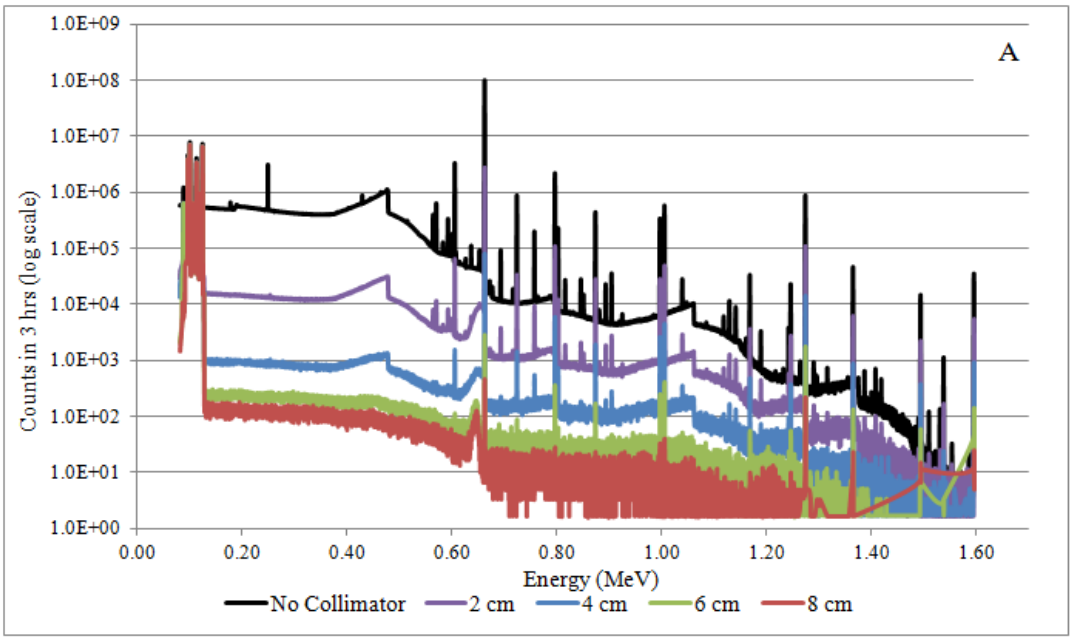

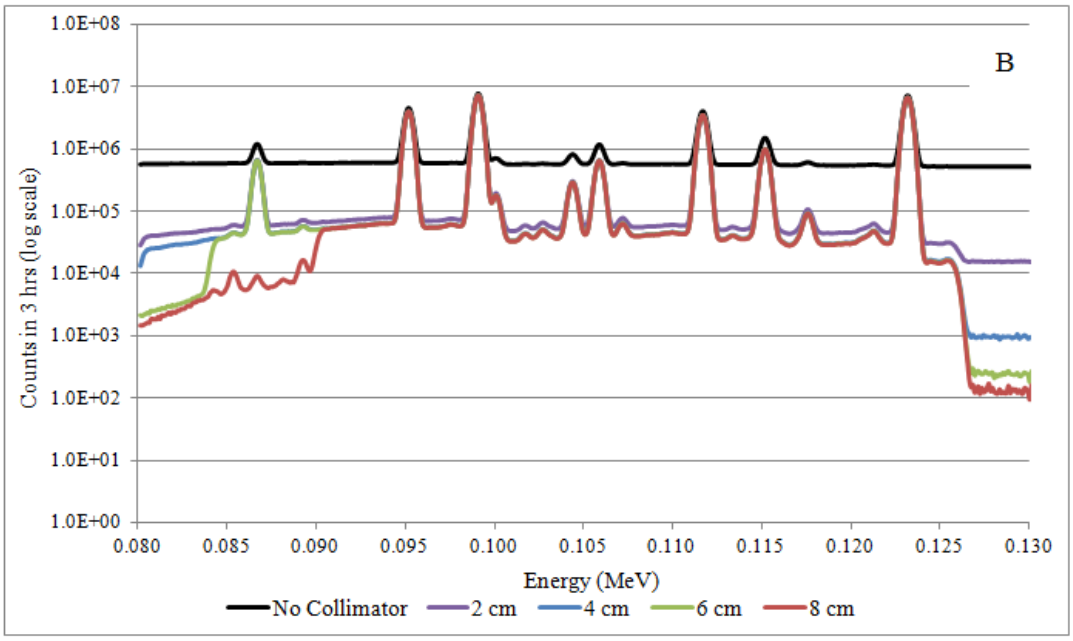

Figure 42. The normalized 3-hour count MCNP F8 tally comparing tungsten collimator lengths (8 cm to 0 cm) to determine the improved signal-to-noise ratio. (A) The high-energy range (0-1.6 MeV) and (B) the energy range of interest (80-125 keV)

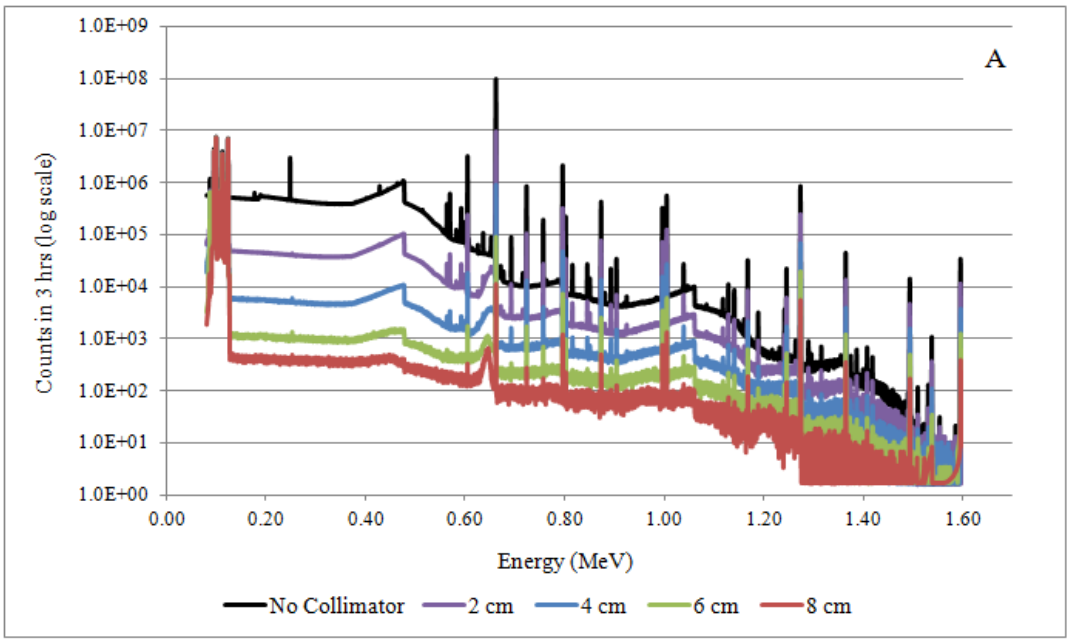

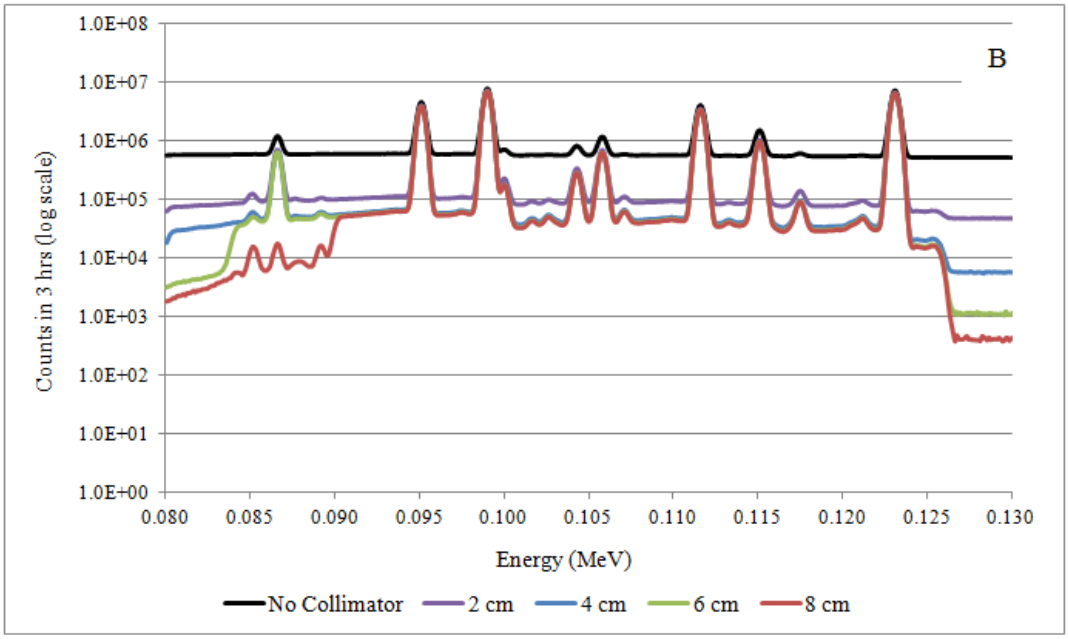

Figure 43. The normalized 3-hour count MCNP F8 tally comparing lead collimator lengths (8 cm to 0 cm) to determine the improved signal-to-noise ratio. (A) The high-energy range (0-1.6 MeV) and (B) the energy range of interest (80-125 keV)

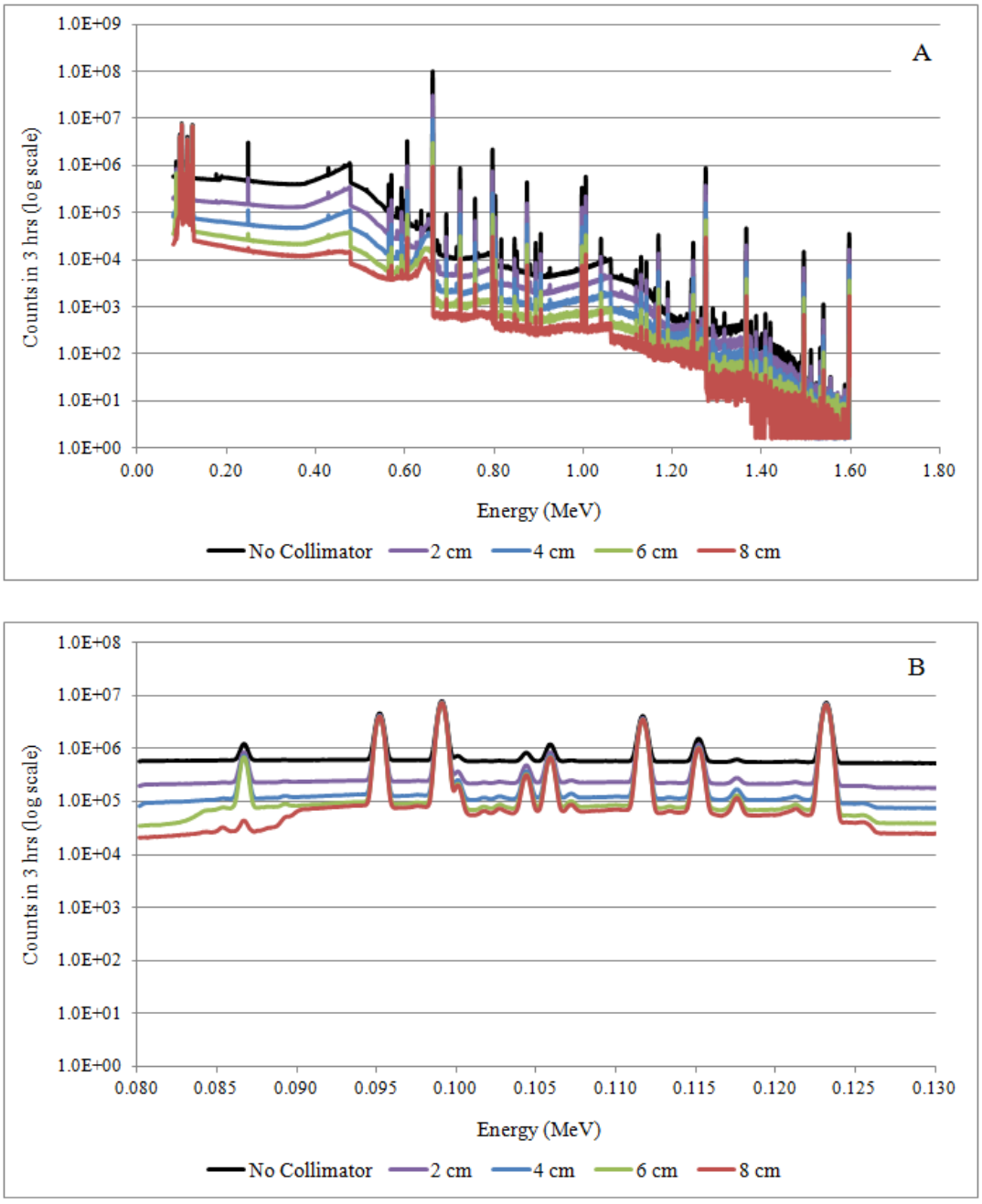

Figure 44. The normalized 3-hour count MCNP F8 tally comparing stainless steel collimator lengths (8 cm to 0 cm) to determine the improved signal-to-noise ratio. (A) The high-energy range (0-1.6 MeV) and (B) the energy range of interest (80-125 keV)

From a visual inspection of the tungsten collimator length comparison, in the energy range of interest (80-125 keV), the 8 cm, 6 cm and 4 cm long collimators offered comparable counts (Fig. 42). The 2 cm collimator data (purple), seen rising slightly above the longer collimator lengths, did not provide the same amount of background suppressment. In the high-energy range, the ability of the collimator to block the high-energy photons was evident. As expected, the simulation without the conic collimator had the greatest number of high-energy photons reach the detector. These counts decreased with increasing collimator length. Therefore, the flat quartz-crystal x-ray spectrometer system was performing as desired. The x-ray energies of interest were diffracted by the crystal and were able to traverse the customized collimation system. The undesired high-energy photons were not diffracted by a large enough Bragg angle to traverse the collimator system. Instead, they interacted with the conic collimator and were attenuated before reaching the HPGe detector. This decreased the amount of background radiation recorded by the detector and reduced the overall Compton continuum underneath the XRF peaks of interest in the 80-125 keV energy range.

Similar results were obtained for the collimator materials of lead and stainless steel. The effectiveness of the collimator and shielding system depended on the density of the collimator material. Therefore, with decreasing density more high-energy photons were able to reach the detector and cause background counts.

The lead and stainless steel collimation systems performed adequately and significantly blocked the high-energy photons from reaching the detector. The

customized conic collimator allowed the diffracted x rays of interest to reach the detector unattenuated.

Additionally, the 86 keV peak visible in the MCNP spectra for the conic collimator with lengths of 6 cm, 4 cm, 2 cm and 0 cm was due to low-energy radiation being able to navigate the length of the conic collimation system. Lower-energy photons were diffracted by a greater angle and were blocked by the 8 cm conic collimator. However, the shorter conic collimators allowed the diffracted 86 keV photons to reach the HPGe detector unattenuated.

From Figures 42-44, the 8-cm long collimator for all of the materials performed best by blocking the highest number of high-energy photons from reaching the detector and thereby contributing to background. The simulated 3-hour counts for the three 8-cm collimators were compared to quantify their affect on improving the signal-to-noise ratio and decreasing the peak percent error of the 103.7 keV Pu x-ray peak (Fig. 45).

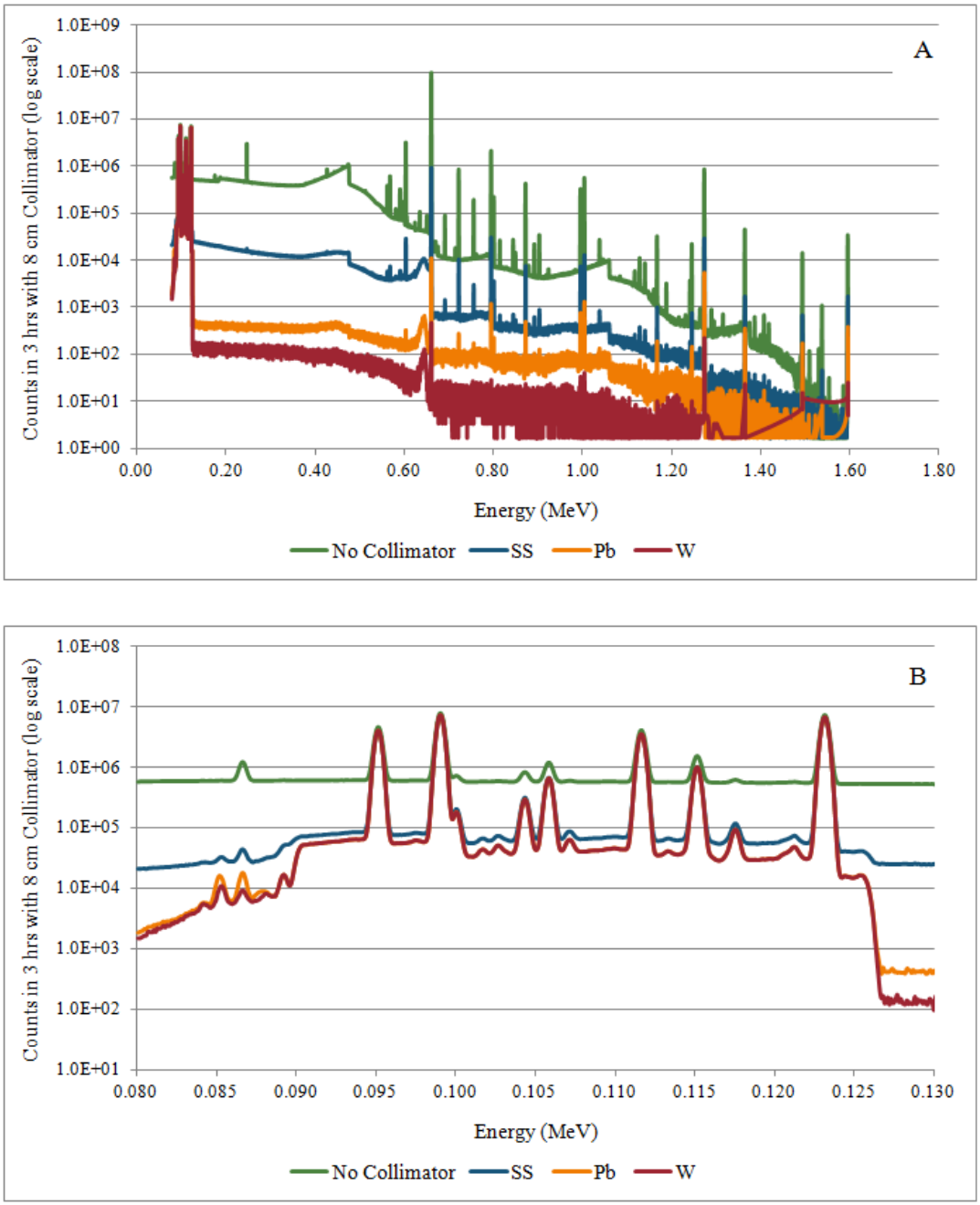

Figure 45. Plot of normalized 3-hour count MCNP F8 tally for 8-cm collimator lengths for collimator materials tungsten, lead and stainless steel compared to the system without a collimator. (A) The high-energy range (0-1.6 MeV) and (B) the energy range of interest (80-125 keV)

The normalized MCNP simulation data for the three collimator materials were entered into Genie2000 such that the photopeaks of interest could be quantitatively analyzed. Using the Genie2000 Interactive Peak Fit software, the photopeak, error and continuum counts for the 103.7 keV Pu and 95 keV U x rays were found (Table XI).

Table XI. Data from MCNP evaluated using Genie2000 for the 103.7 keV Pu x-ray peak and the 95 keV U x-ray peak for a simulated 3-hour count for three 8-cm long collimator materials: tungsten, lead and stainless steel

Collimator Material	103.7 keV Pu x ray			95 keV U x ray		
	Photopeak (counts)	Error (counts)	Continuum (counts)	Photopeak (counts)	Error (counts)	Continuum (counts)
W	1.35E+06	3055	7.99E+05	2.21E+07	7272	1.87E+06
Pb	1.35E+06	3062	8.03E+05	2.21E+07	6270	1.38E+06
SS	1.36E+06	3523	1.16E+06	2.21E+07	6876	1.94E+06
None	1.35E+06	10293	1.04E+07	2.21E+07	14013	1.39E+07

From the recorded 103.7 keV Pu photopeak, error and continuum counts, the signal-to-noise ratio and percent error were calculated (Table XII). The data were used to quantitatively determine the improvement of the signal-to-noise ratio and change in percent error. To calculate the improved signal-to-noise ratio and the ratio of percent error, the data for the three collimator materials data were compared to the system without the conic collimator. Also, the 95 keV U x-ray peak counts were used with the Pu data to calculate the Pu to U ratio from the simulation results (Table XII).

Use of the collimation system significantly improved the signal-to-noise ratio for the 103.7 keV Pu x-ray peak. Tungsten was found to be the optimal collimator material and improved the signal-to-noise ratio by a factor of 13 compared to the system without the secondary conic collimator. This was expected as tungsten represented the most dense and therefore best shield against high-energy photons. The lead conic collimator was a close second producing an improved signal-to-noise ratio of 12.95 times. Even the stainless steel collimator provided a significant improvement of 9 times over the system lacking the conic collimation system.

Also, the Pu to U peak ratio did not change significantly in each simulation (Table XII). These values need to be benchmarked against experiment.

Table XII. The simulated signal-to-noise ratios and percent errors for the 103.7 keV Pu $K_{\alpha 1}$ x-ray peak and the 103.7 keV Pu peak to 95 keV U peak ratio were found with and without the collimator

Collimator Material	103.7 keV Pu x ray				103.7 keV Pu to 95 keV U Peak Ratio
	Signal-to-Noise Ratio	Percent Error	Improved Signal-to-Noise Ratio	Ratio of Percent Error	
W	1.69 ± 0.01	0.23%	13.02 ± 0.10	0.30	0.0611 ± 0.0001
Pb	1.68 ± 0.01	0.23%	12.95 ± 0.10	0.30	0.0611 ± 0.0001
SS	1.17 ± 0.01	0.26%	9.03 ± 0.07	0.34	0.0615 ± 0.0002
None	0.13 ± 0.01	0.76%			0.0611 ± 0.0005

Several assumptions were made for the simulation:

- No impurities or defects within the crystal were considered such that all photons were diffracted perfectly by the flat quartz crystal
- The cold finger and dewar for the HPGe detector were neglected
- β-particle contributions to XRF were neglected as they were previously shown to represent only ~20% of the XRF source and did not change the Pu to U ratio[1,2]

Therefore, from an analysis of the MCNP simulations and the October 2011 ORNL measurement campaign data, a comparable percent error in the 103.7 keV Pu x-ray peak from an 18-hour count using the original detection system (Fig. 28) could be obtained from a 3-hour count using the flat quartz-crystal x-ray spectrometer and secondary conic collimation systems. The ability of the crystal to diffract the x rays of interest and of the conic collimation system to block the unwanted, high-energy background radiation from reaching the HPGe detector significantly decreased the recorded Compton background while optimizing the x ray detection. However, these results must be confirmed with experiment.

5.2 Natural Uranium Simulation

Before using the flat quartz-crystal x-ray spectrometer to measure spent fuel, experimenters may first want to test the system capabilities by performing lab scale measurements. Instead of using SNF, another option is to use a natural uranium source. The XRF from a natural U source would interact with the crystal and be diffracted outward conically. Using the same or similar customized collimation system, the x-rays of interest from U can be recorded. To increase the count rate from the U source, another radioactive source can be used as a stimulant to induce XRF. Two stimulant sources were evaluated: ^{137}Cs and barium-133 (^{133}Ba).

5.2.1 Geometry and Source Definition

The natural uranium sources available at Texas A&M University are uranium standards of natural ore (U_3O_8)[25]. The ^{235}U isotopic abundance in natural U is 0.72%. The density of U_3O_8 is approximately 2.07 g/cc. Also, since XRF does not measure the individual isotopes of an element, but rather the bulk elemental content, any U standard (depleted, natural or enriched) would work equally well. The dimensions of the U standard canister were known and can be found in Appendix C.

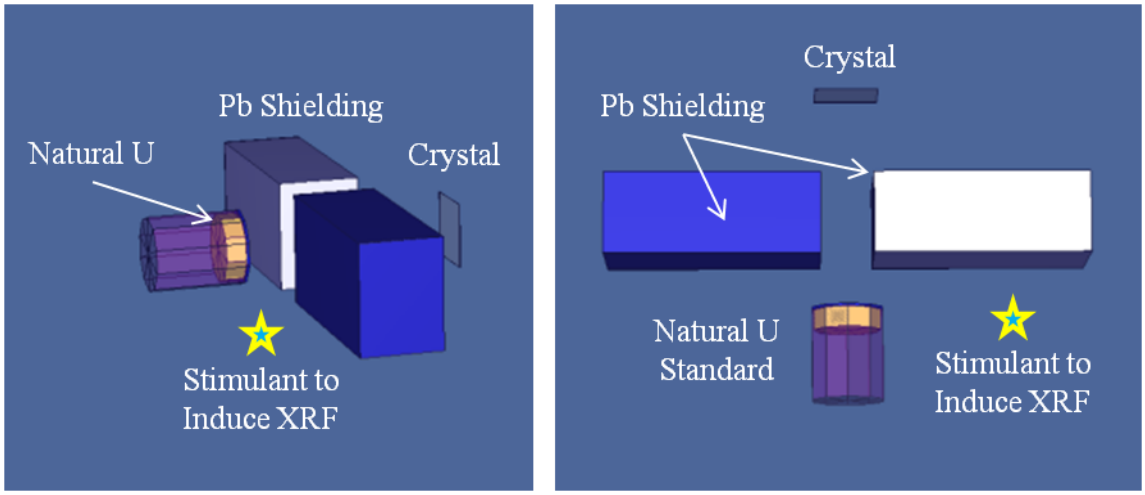

Figure 46. The primary MCNP natural uranium simulation geometry where ^{137}Cs and ^{133}Ba were used to induce XRF (not to scale)

MCNP was used to simulate induced XRF from a uranium standard (Fig. 46). The canister was modeled in MCNP according to the reference dimensions[25]. The uranium was sealed in an Al canister. The thickness of the U ore was approximately 2 cm with a radius of 3.2 cm. The outer Al canister was approximately 9 cm long with a radius of 3.5 cm[25]. To model the induced XRF from the ^{137}Cs and ^{133}Ba sources, a point source was introduced into the simulation. Two simulations were performed. The first simulation was of the XRF from the U can directly onto a tallying surface. The ^{137}Cs and ^{133}Ba source stimulants were positioned behind Pb shielding such that their photopeaks would not contribute to background counts.

The second simulation took the output tally data from the first simulation and used it to create the x-ray diffraction source from the analyzing crystal. To replicate x-ray diffraction in MCNP, an energy-direction coupled source definition was used. This

allowed for a specific energy photon to be oriented in a desired direction. The conic collimator described in Section 4 was used.

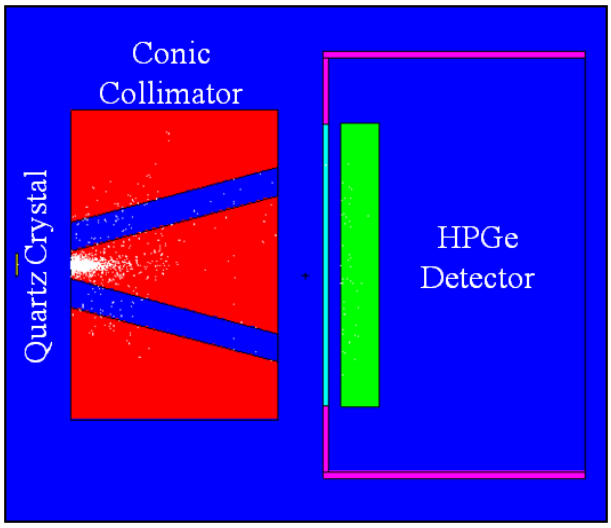

Figure 47. An image from VisEd of photons attempting to traverse the conic collimator system with the majority of the high-energy photons being attenuated due to insufficient angular diffraction

5.2.2 Simulation Analysis

First, the primary simulation was conducted to record the natural uranium spectra. The energy and counts data were recorded using an F2 surface flux tally on the crystal surface. This F2 tally information was used in the secondary simulation as the source definition. The flat, transmission-type crystal diffracted the uranium x rays outward conically. The diffraction was replicated in MCNP using a card which defined the photon direction according to its energy. As the tungsten collimator was found to be the most effective collimator from the spent fuel measurements, it was used again for the

natural ore simulations. Simulations for collimator lengths of 8 cm, 6 cm, 4 cm, 2 cm and none were compared to quantify the reduction in background due to the conic collimator.

The first MCNP simulation did not include the conic collimator. The results from this simulation were used to determine the effect the collimator had on reducing the Compton background and unwanted photons from reaching the detector. The MCNP simulation without the conic collimator system was analyzed using Genie2000 to determine the peaks present (Fig. 48).

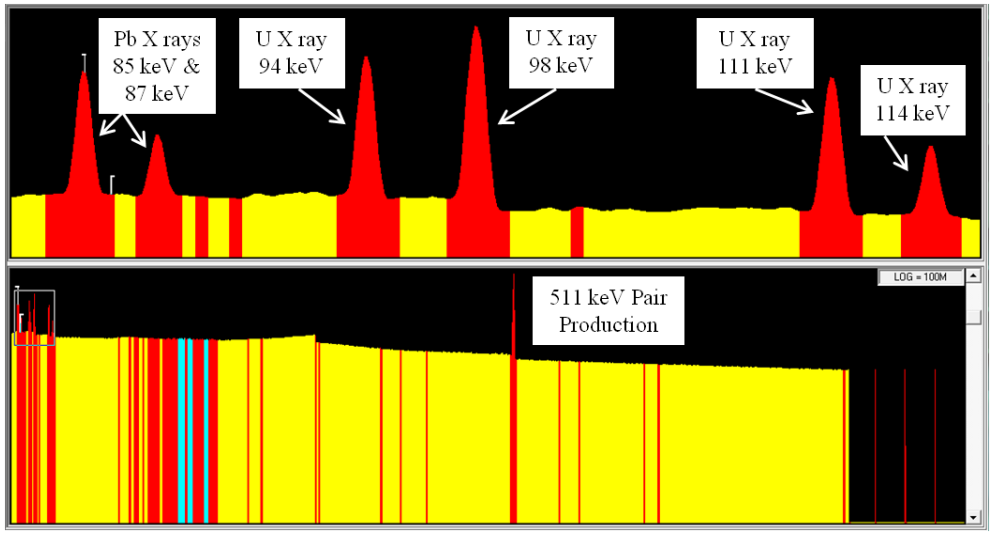

Figure 48. The MCNP simulated induced XRF from natural U ore using the ^{133}Ba F8 output data without the conic collimator was input into Genie2000 to analyze the visible peaks

The ^{133}Ba induced XRF plots were not normalized to any experimental data. Instead, the MCNP data offers a representation of the expected photon spectra recorded

when measuring induced XRF from natural U ore. From the Genie2000 data, the signal-to-noise ratio and peak percent error of the 95 keV U x ray were calculated (Table XIII).

Table XIII. MCNP data were evaluated using Genie2000 for the 95 keV U x-ray peak for the XRF from natural U ore stimulated by a ^{133}Ba source with the W conic collimator

Collimator Length (cm)	Photopeak (counts)	Error (counts)	Continuum (counts)	Signal-to-Noise Ratio	Percent Error (%)
8	1.06E+07	6376	2.31E+06	4.59	0.06%
6	1.06E+07	6376	2.31E+06	4.59	0.06%
4	1.06E+07	3681	2.31E+06	4.59	0.03%
2	1.06E+07	6265	2.28E+06	4.65	0.06%
None	1.06E+07	9584	5.99E+06	1.77	0.09%

The natural U ore simulations did not include the high background radiation levels observed in the spent fuel simulations. Still the effectiveness of the conic collimator in increasing the signal-to-noise ratio of the x-ray peak of interest was clear. The 8-cm, 6-cm, 4-cm and 2-cm tungsten conic collimators all improved the signal-to-noise ratio of the 95 keV U x ray by over 4.5 times. The main contributor to high-energy background radiation came from high-energy U gamma rays.

From a visual inspection of Figure 49, the tungsten collimator successfully shields the HPGe detector from the majority of the high-energy gammas. The results from the ^{137}Cs induced XRF simulations were very similar to the ^{133}Ba results. Therefore, this simple simulation using natural ore as the U XRF source has shown that

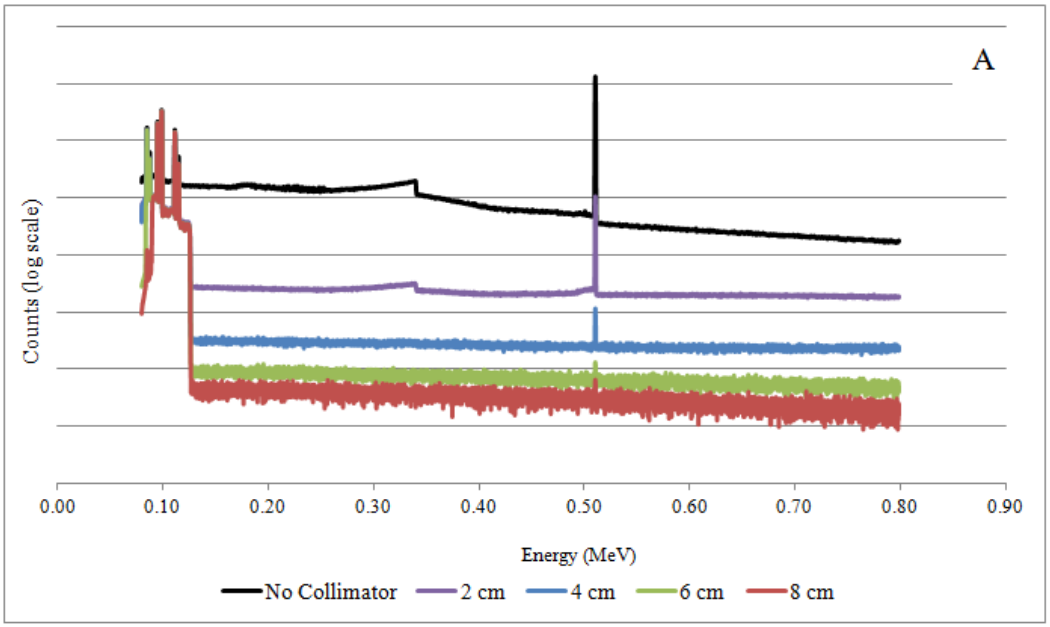

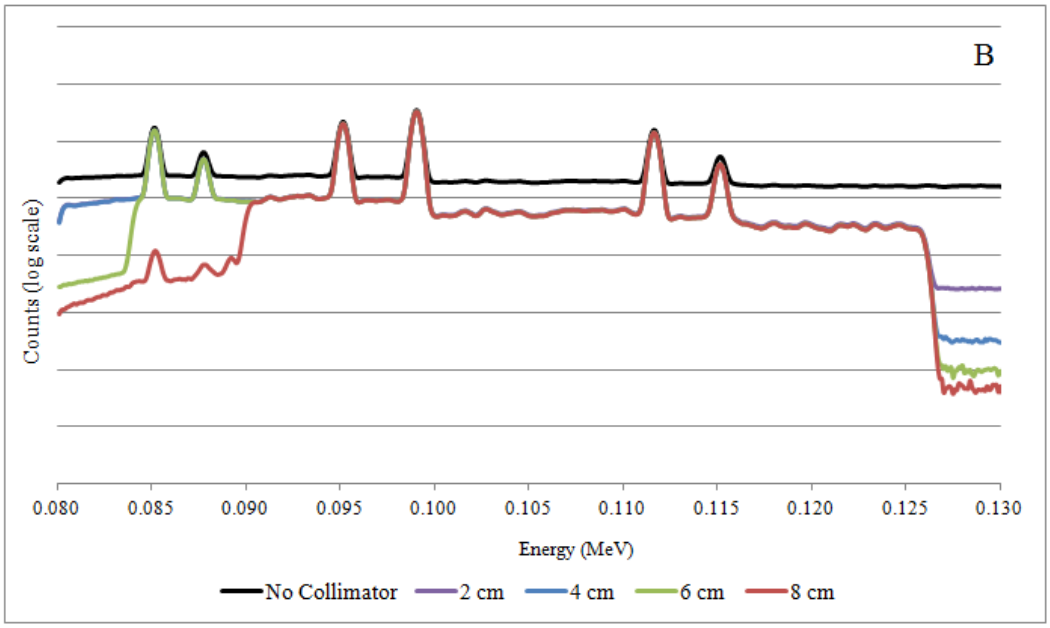

Figure 49. Plot of the secondary simulation MCNP F8 tally of the XRF from natural U ore induced by a ^{133}Ba source comparing the tungsten collimator lengths. (A) The high-energy range (0-800 keV) and (B) the energy range of interest (80-125 keV)

lab-scale experiments using the flat quartz-crystal x-ray spectrometer could be performed successfully before using it to measure XRF from SNF in a hot cell laboratory.

5.3 Simulation Results Overview

Overall, the MCNP simulations successfully illustrated the potential of the flat quartz-crystal x-ray spectrometer in improving the detection capability of the Pu to U XRF peak ratio.

For the spent fuel simulations, the MCNP simulations were scaled to the October 2011 ORNL SNF 3-hour measurements. The simulations found that the tungsten and lead 8-cm collimators, when used with the flat quartz-crystal x-ray spectrometer system, improved the 103.7 keV Pu $K_{\alpha 1}$ x-ray peak signal-to-noise ratio by a factor of 13 as compared to the original, undiffracted and unshielded simulation. Also, the simulations determined that the crystal x-ray spectrometer system decreased the peak percent error of the 103.7 keV peak by 3.33. The SNF simulations must be benchmarked against experimental results.

Other simulations using natural U ore as the XRF source were performed to determine how the crystal x-ray spectrometer system would operate in a lab-scale experiment. The tungsten collimator appreciably decreased the Compton background counts, thereby increasing the signal-to-noise ratio of the Pu x-ray peak of interest by a factor of about 4.5. The natural U ore simulations must be benchmarked against experimental results.

5.4 Flat Quartz-Crystal X-ray Spectrometer System Overview

The overall design specifications for the proposed flat quartz-crystal x-ray spectrometer follow in Figure 50.

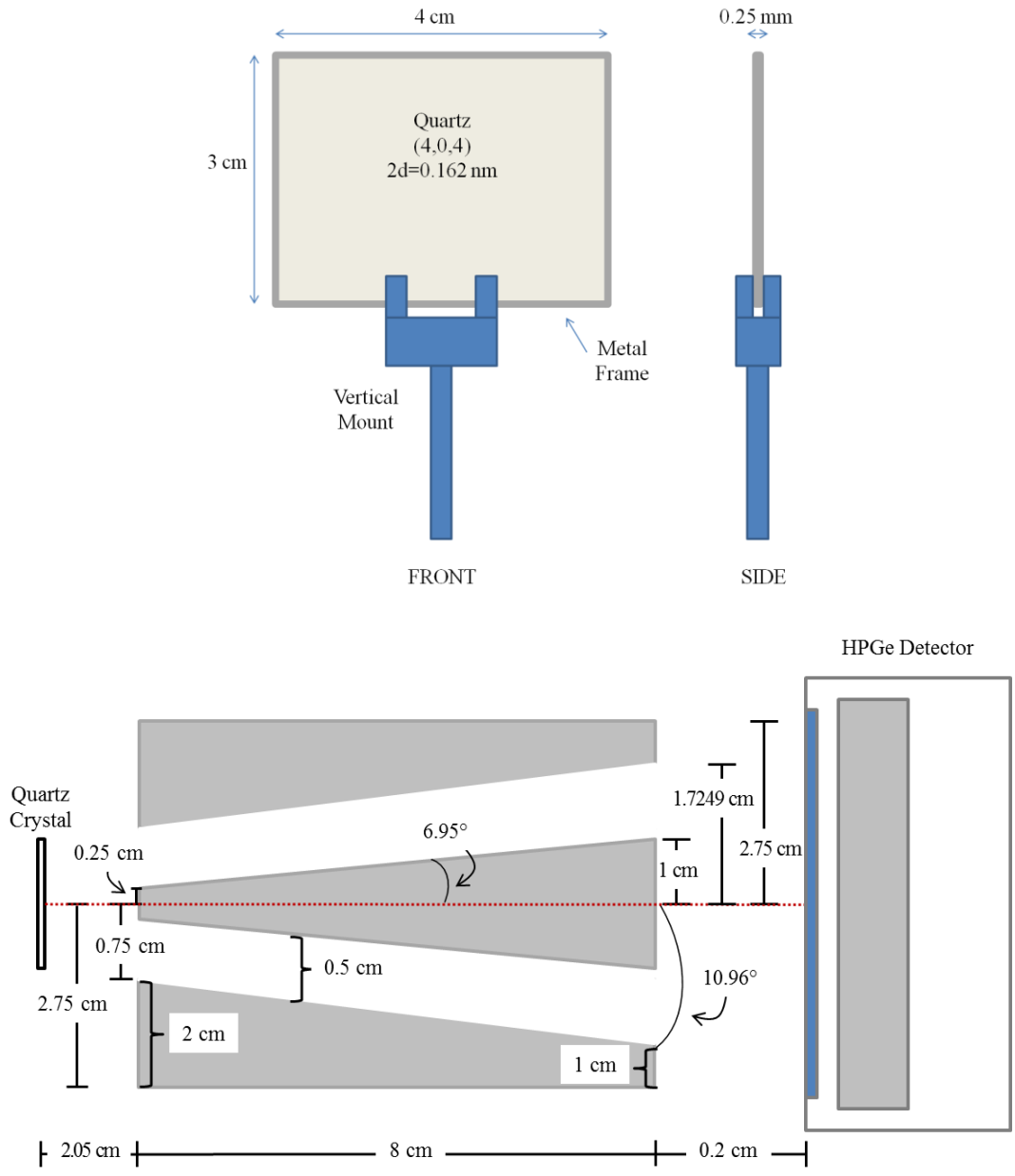

Figure 50. The overall crystal x-ray spectrometer and conic collimation system designs

The transmission-type, flat quartz-crystal x-ray spectrometer dimensions are 3 cm tall by 4 cm wide by 0.025 cm thick (Fig. 50). The interplanar spacing of the (4,0,4) cut crystal is 0.1624 nm. A metal frame, potentially made of Al, surrounds the crystal to allow for a vertical mount to grip the crystal.

The secondary conic collimator system is composed of an inner conic collimator and an outer shield. The dimensions of the secondary collimator are shown in Figure 50. The customized secondary collimator allows only x rays diffracted by an angle within the energy range of interest (80-125 keV) to successfully traverse the collimator and hit the HPGe detector.

MCNP simulations showed that the use of the flat quartz-crystal x-ray spectrometer system with no conic collimator versus the 8-cm long tungsten conic collimator system would increase the signal-to-noise ratio of the 103.7 keV Pu $K_{\alpha 1}$ x-ray peak from 0.13 to 1.69. Additionally the percent error of the 103.7 keV peak would decrease from 0.76% to 0.23%. The MCNP simulation results were scaled to a 3-hour SNF measurement. However, this improvement would correspond to a substantially longer count time in the original measurement campaign when not using the crystal x-ray spectrometer and conic collimator systems. The original measurements allowed all of the unwanted high-energy photons to reach the HPGe detector and produce background counts in the energy region of interest. The improved signal-to-noise ratio of the 103.7 keV peak was basically unreachable without using the crystal x-ray spectrometer and conic collimation systems.

While these simulation results were originally scaled to experimental data from ORNL, the results only offer a proof-of-concept solution and must be benchmarked to experimentally obtained results. The potential of the crystal x-ray spectrometer and conic collimator systems is clear from the improved signal-to-noise ratio and decreased peak percent error obtained from the MCNP simulations. With these improvements, the required count times when performing photon spectroscopy on SNF could be decreased. The decrease in required count time would greatly benefit scientists performing the technical nuclear forensics technique of XRF measurements on interdicted SNF samples.

6. CONCLUSIONS

The October 2011 Three Mile Island spent nuclear fuel measurement campaign at Oak Ridge National Laboratory confirmed that the 103.7 keV Pu to 95 keV U x-ray ratio could be measured from a spent fuel rod using a planar HPGe detector. However, these measurements also demonstrated that the significant background continuum caused by the incoherent scattering of high-energy photons from the fuel partially obscured the Pu peak. A method to decrease the Compton background recorded by the HPGe detector was researched by investigating the use of a flat quartz-crystal x-ray spectrometer. This wavelength-dispersive spectroscopy technique isolated the photon energy range of interest (80-125 keV) from the majority of the collimated beam. By preferentially detecting photons from the energy range of interest while blocking unwanted gammas from reaching the detector, the Compton background was reduced.

Overall, from proof-of-concept MCNP simulations the flat quartz-crystal x-ray spectrometer and conic collimation systems were shown to dramatically increase the signal-to-noise ratio of the 103.7 keV Pu x-ray peak of interest. The use of a flat-quartz crystal to diffract incident x rays presents a simple, repeatable and passive method of measuring a narrow energy band of radiation from an energetically heterogeneous source. The selected flat quartz crystal was optimized for the measurement of the 103.7 keV Pu and 95 keV U x rays. The crystalline structure and crystal thickness were chosen to optimize diffraction of the desired x-ray energies by a significant Bragg angle. The dimensions of the crystal were determined from restraints and requirements found

when performing measurements in a hot cell laboratory, such as the ORNL Irradiated Fuels Examination Lab.

The conic collimation system was customized to allow only photons in the energy range of interest (80-125 keV) to successfully reach the HPGe detector. The collimation system was designed specifically to work with a low-energy HPGe detector with a Ge crystal radius of 2.523 cm, thickness 15 mm and 0.5-mm thick Be window. Collimator lengths of 8 cm, 6 cm, 4 cm and 2 cm were considered. Collimator materials considered were tungsten, lead and stainless steel.

Multiple MCNP simulations were performed to quantitatively determine the effect of the flat quartz-crystal spectrometer on the background counts. Different lengths and materials were modeled in MCNP. The most dense materials, tungsten and lead, were found to most efficiently attenuate the high-energy photons. These materials resulted in the most improved 103.7 keV Pu x ray signal-to-noise ratio and reduced peak percent error ratio of approximately 13x and 0.3, respectively. To prepare for a preliminary tabletop scale experiment, simulations were performed using natural U irradiated by ^{133}Ba and ^{137}Cs and the optimized tungsten collimator system. An analysis of the simulation results showed that the signal-to-noise ratio of the Pu 103.7 keV x-ray peak was improved by approximately 4.6 times using the flat quartz-crystal x-ray spectrometer and customized collimator systems. As there was not as much background radiation present in the natural U simulations, the signal-to-noise ratio did not increase as drastically as when implemented in the SNF simulations using the crystal and collimation systems.

Future work for this project includes acquiring the proposed flat quartz crystal and manufacturing the secondary conic collimator system to benchmark the simulations. To accurately determine the signal-to-noise ratio improvement and the decrease to the peak percent error, experiments using the systems must be performed. First, lab-scale XRF measurements from U standards should be carried out as described in the simulations. Once the properties of the crystal x-ray spectrometer system have been characterized, spent fuel measurements should be attempted at ORNL. Additional wavelength-dispersive spectroscopy techniques for the purpose of reducing background radiation in the HPGe detector should also be investigated, including multilayer x-ray mirrors.

REFERENCES

1. A.S. STAFFORD, "Spent Nuclear Fuel Self-Induced XRF to Predict Pu to U Content," M.S. Thesis, Texas A&M University, College Station (2001).

2. C. FREEMAN, V. MOZIN, S. TOBIN, M. FENSIN, J. WHITE, A.S. STAFFORD, W.S. CHARLTON and S. CROFT, "Feasibility of X-Ray Fluorescence for Spent Fuel Safeguards," Los Alamos National Laboratory LA-UR-10-04736 (2010).

3. K.J. MOODY, I.D. HUTCHEON and P.M. GRANT, *Nuclear Forensics Analysis*, Taylor & Francis, Boca Raton, FL (2005).

4. A.V. BUSHUEV, V.I. GALKOV, A.V. ZBONAREY, A.F. ZOLOTOV, A.A. KUTUZOV, M.A. MEL'NICHENKO, V.N. OZERKOV and V.V. CHACHIN, "A Nondestructive Method of Determining the Pu/U Ratio in Fast Reactor Fuel Elements, Based on X-Ray Spectrometry," *Atomic Energy*, **53**, 5 (1982).

5. C. RUDY, P. STAPLES, K. SEREKNIUK and I. YAKOVLEV, "Determination of Pu in Spent Fuel Assemblies by X-Ray Fluorescence," *Proceedings of 46th Annual Meeting of the INMM*, Phoenix, AZ (July 10-14, 2005).

6. "TransFXTM Computer Software Manuals: Advanced Particle Transport Software Using Three-Dimensional Deterministic Methods in Arbitrary Geometry," TransWare Enterprises Inc. (2001).

7. W.S. CHARLTON, D. STROHMEYER, A.S. STAFFORD, S. SAAVEDRA, A.S. HOOVER and C. RUDY, "The Use of Self-Induced XRF to Quantify the Pu Content in PWR Spent Nuclear Fuel," *Proceedings of 31st Annual Meeting of ESARDA*, Vilnius, Lithuania (May 26-28, 2009).

8. Evaluated Nuclear Data File ENDF/B-7.1, Cross Section Evaluation Working Group, Brookhaven National Laboratory (2011).

9. D. REILLY, N. ENSSLIN and H. SMITH, *Passive Nondestructive Assay of Nuclear Materials*, Washington, DC, NUREG-CR/5550 (1991).

10. R.J.D. TILLEY, *Crystals and Crystal Structures*, John Wiley & Sons, England (2006).

11. J.L. AMOROS, M.J. BUERGER and M.C. DE AMOROS, *The Laue Method*, Academic Press, New York (1975).

12. R.E. VAN GRIEKEN and A.A. MARKOWICZ, *Handbook of X-Ray Spectrometery* 2nd Edition, Marcel Dekker, New York (2002).

13. M.A. BLOKHIN, *Methods of X-Ray Spectroscopic Research*, Pergamon Press, New York (1965).

14. Y. CAUCHOIS, *Les Spectres de Rayons X et la Structure Electronique de la Matiere*, Centre National de la Recherche Scientifique, Paris (1948).

15. J.W.M. DUMOND, "Gamma-Ray Spectroscopy by Direct Crystal Diffraction," *Annual Review Nuclear Science*, **8**, pp. 163-165 (1958).

16. M. PIVOVAROFF, "X-ray Optics for Astrophysics and Free Electron Lasers," Lawrence Livermore National Laboratory LLNL-PRES-403477 (2008).

17. M. PIVOVAROFF, "Hard X-ray Optics for Astronomy and the Laboratory," *Workshop on Emerging Scientific Opportunities Using X-ray Imaging*," Fontana, WI (2004).

18. E.O. BARANOVA and M.M. STEPANEKNO, "Cauchois-Johansson X-Ray Spectrograph for 1.5-400 keV Energy Range," *Review of Scientific Instruments*, **72**, 2 (2001).

19. J.W. KNOWLES, "Crystal Diffraction Spectrometers," *Nuclear Instruments and Methods*, **162**, pp. 677-680 (1979).

20. G.F. KNOLL, *Radiation Detection and Measurement* 3rd Edition, John Wiley & Sons, New York (2000).

21. R. JENKINS and J.L. DE VRIES, *Practical X-Ray Spectrometry* 2nd Edition, Springer-Verlag, New York (1970).

22. "Low Energy Germanium Detectors (GL)." Canberra AREVA; www.canberra. com/products/493.asp/.

23. A.G. Croff, "A User's Manual for ORIGEN2 Computer Code," ORNL/TM-7175 (1980).

24. "MCNP – A General Monte Carlo N-Particle Transport Code Version 5 Manual." Los Alamos National Security, 2005.

25. "SRM: Uranium-235 Isotope Abundance Standard Reference Materials for Gamma Spectrometry Measurements," National Bureau of Standards, (1986).

APPENDIX A

Table with the dimensions of the 8-cm, 6-cm, 4-cm and 2-cm long conic collimation system:

Cone Length: 8 cm						
x1 =	2.050	cm		x2 =	8.00	cm
y_0 =	0.25	cm		y_1 =	1.2255	cm
y_3A =	0.75	cm		y_gap =	0.5	cm
y_3B =	2.75	cm		y_t1 =	2.0	cm
y_4A =	1.7249	cm		y_t2 =	1.0	cm
y_4B =	2.75	cm				
Cone Length: 6 cm						
x1 =	2.050	cm		x2 =	6.00	
y_0 =	0.25	cm		y_1 =	0.9816	
y_3A =	0.75	cm		y_gap =	0.5	cm
y_3B =	2.75	cm		y_t1 =	2.0	cm
y_4A =	1.4816	cm		y_t2 =	1.0	cm
y_4B =	2.75	cm				
Cone Length: 4 cm						
x1 =	2.050	cm		x2 =	4.00	cm
y_0 =	0.25	cm		y_1 =	0.7378	cm
y_3A =	0.75	cm		y_gap =	0.5	cm
y_3B =	2.75	cm		y_t1 =	2.0	cm
y_4A =	1.2378	cm		y_t2 =	1.0	cm
y_4B =	2.75	cm				
Cone Length: 2 cm						
x1 =	2.050	cm		x2 =	2.00	cm
y_0 =	0.25	cm		y_1 =	0.4939	cm
y_3A =	0.75	cm		y_gap =	0.5	cm
y_3B =	2.75	cm		y_t1 =	2.0	cm
y_4A =	0.9939	cm		y_t2 =	1.0	cm
y_4B =	2.75	cm				

APPENDIX B

MCNP deck of the 8-cm long, lead conic collimation system with the energy-direction coupled source definition (the source definition is abbreviated):

```
Collimator Test
C     SDEF: SNF 7o6 (F2 tally)
C     Collimator: Pb cone, Length: 8 cm
C     Beam source: point source at (0,0,0) in +x direction
C     Energy bandgap: 90 keV - 125 keV
C     NPS: 5B
C
C     ------------------
C     --- Cell cards ---
C     ------------------
C     Bent crystal
1     52 -2.65     +1 -2 -3 +4 -5 +6          imp:p=1
C     Secondary collimator: conic, tungsten
10    11 -11.34    -10                        imp:p=1      $ Pb cone
11    50 -1.2e-3   -11 +10                    imp:p=1      $ Air region
12    11 -11.34    -12 +11                    imp:p=1      $ Outer Pb coll
C     HPGe detector
30    103 -2.7     +33 -32 +20 -36            imp:p=1      $ Al can
31    103 -2.7     -33 +34 +20 -35            imp:p=1      $ Front Al
32    101 -1.85    -34 +20 -35                imp:p=1      $ Be window
33    100 -5.32    -40 +41 -42                imp:p=1      $ HPGe detector
34    50  -1.2e-3  -33 +35 -36 #33            imp:p=1      $ Air in detector
C     Void
100   50  -1.2e-3  #1 #10 #11 #12 #30 #31 #32 #33 #34 -100   imp:p=1
C     Universe
999   0            +100                                     imp:p=0

C     ---------------------
C     --- Surface cards ---
C     ---------------------
C     Bent crystal
1     px -0.1
2     px +0.0
3     py +0.2
4     py -0.2
5     pz +0.2
6     pz -0.2
C
C  (x,y,z) coords of bottom, (Hx,Hy,Hz) cone axis height, base & upper rad
10    TRC +2.05 0 0  +8.0 0 0  +0.25 +1.2255
11    TRC +2.05 0 0  +8.0 0 0  +0.75 +1.7255
12    TRC +2.05 0 0  +8.0 0 0  +2.75 +2.751
C
20    px +11.835
C
C     HPGe Detector System
```

```
32    cx +3.8       $ Outer Al shell
33    cx +3.67      $ Inner Al shell
34    cx +2.5       $ Be Window
35    px +12.015    $ Window end cut
36    px +22        $ Al can back
40    cx +2.52      $ HPGe radius - Canberra GL2015R
41    px +12.515    $ Air in detector cut
42    px +14.015    $ HPGe back cut
C
C     Universe
100   sx +10 +15

C     ------------------
C     --- Data cards ---
C     ------------------
MODE P
C    Material 10: Natural Tungsten (19.28 g/cc)
m10  74182 0.268
     74183 0.143
     74184 0.3067
     74186 0.286
C    Material 11: Lead (11.34 g/cc)
m11  82000 1.0
C    Material 50: Air (1.2e-3 g/cc)
m50  7014  -0.755              $ N
     8016  -0.232              $ O
     18000 -0.013              $ Ar
C    Material 52: Quartz (2.66 g/cc)
m52  14000 -1                  $ Si
     8016  -2                  $ O2 : Quartz bent crystal
C    Material 100: HPGe (5.32 g/cc)
m100 32000. 1
C    Material 101: Be (1.85 g/cc)
m101 4009   1
C    Material 102: Stainless Steel 304 (8.03 g/cc)
m102 26000.  -0.6785
     6000.   -0.008   14000.  -0.01   24000.  -0.18
     28000.  -0.098   25055.  -0.018  15031.  -0.0045
     16032.  -0.003
C    Material 103: Aluminum (2.7 g/cc)
m103 13000. 1
C     -------------------
C     --- Source Defn ---
C     -------------------
SDEF SUR=2 POS=0 0 0 VEC=1 0 0 ERG=d1 DIR FERG d2
C     -- Source info: energies (MeV) --
SI1 L 8.0100E-02 3.3352E-01 5.8693E-01 8.4035E-01 1.0938E+00 1.3472E+00
      8.0200E-02 3.3362E-01 5.8703E-01 8.4045E-01 1.0939E+00 1.3473E+00
      8.0300E-02 3.3372E-01 5.8713E-01 8.4055E-01 1.0940E+00 1.3474E+00
      8.0400E-02 3.3382E-01 5.8723E-01 8.4065E-01 1.0941E+00 1.3475E+00
      8.0500E-02 3.3392E-01 5.8733E-01 8.4075E-01 1.0942E+00 1.3476E+00
      8.0600E-02 3.3402E-01 5.8743E-01 8.4085E-01 1.0943E+00 1.3477E+00
```

```
      8.0700E-02 3.3412E-01 5.8753E-01 8.4095E-01 1.0944E+00 1.3478E+00
      8.0800E-02 3.3422E-01 5.8763E-01 8.4105E-01 1.0945E+00 1.3479E+00
                              ------ Cut -------
                  C     -- Source dist: probabilities --
 SP1 D 3.27794E-07 2.25677E-06 3.20434E-06 5.98089E-08 1.84313E-08 1.78674E-09
       3.43685E-07 2.23642E-06 3.15829E-06 5.97307E-08 2.33623E-08 1.72383E-09
       3.46595E-07 2.27017E-06 3.13435E-06 5.79427E-08 2.30296E-08 1.62455E-09
       3.63858E-07 2.28534E-06 3.19658E-06 5.73692E-08 1.73586E-08 2.97274E-09
       3.57971E-07 2.29077E-06 3.21521E-06 5.66887E-08 1.89186E-08 2.45237E-09
       3.57597E-07 2.26611E-06 3.19330E-06 4.72961E-08 1.91218E-08 2.02220E-09
       3.65551E-07 2.23776E-06 3.16353E-06 5.52060E-08 2.34096E-08 1.64340E-09
       3.66569E-07 2.28380E-06 3.20420E-06 5.66038E-08 1.91630E-08 1.58558E-09
       3.61013E-07 2.26710E-06 3.21068E-06 5.74764E-08 1.89564E-08 2.16390E-09
       3.60372E-07 2.27005E-06 3.17986E-06 5.57332E-08 1.82216E-08 1.36171E-09
       3.58615E-07 2.25810E-06 3.17067E-06 5.47935E-08 1.99362E-08 6.60305E-10
       3.57340E-07 2.29431E-06 3.16537E-06 5.73880E-08 2.18311E-08 2.54239E-09
                              ------ Cut -------
C     -- Direction distribution: mu --
DS2 L 0.98180607 0.99895058 0.99966114 0.99983470 0.99990243 0.99993568
      0.98185141 0.99895121 0.99966126 0.99983474 0.99990245 0.99993569
      0.98189658 0.99895184 0.99966137 0.99983478 0.99990247 0.99993570
      0.98194159 0.99895247 0.99966149 0.99983482 0.99990248 0.99993571
      0.98198643 0.99895310 0.99966160 0.99983486 0.99990250 0.99993572
      0.98203110 0.99895372 0.99966172 0.99983490 0.99990252 0.99993573
      0.98207560 0.99895435 0.99966183 0.99983494 0.99990254 0.99993574
      0.98211994 0.99895497 0.99966195 0.99983498 0.99990255 0.99993575
      0.98216412 0.99895560 0.99966206 0.99983501 0.99990257 0.99993576
                              ------ Cut -------
      0.99894743 0.99966056 0.99983450 0.99990234 0.99993563
      0.99894806 0.99966068 0.99983454 0.99990236 0.99993564
      0.99894869 0.99966079 0.99983458 0.99990238 0.99993565
      0.99894932 0.99966091 0.99983462 0.99990239 0.99993566
      0.99894995 0.99966103 0.99983466 0.99990241 0.99993567
C
C     ------------------
C     Pulse height tally
C     ------------------
F8:p 33
E8 0 0.001 0.08 15198i 1.6
FT8 GEB -0.00056627 0.00438995 -3.85265
C
NPS 5e9
```

APPENDIX C

Natural Uranium Ore Standard

Figure 1. ^{235}U Isotope Abundance Certified Reference Material Samples for Non-destructive Gamma Spectrometry

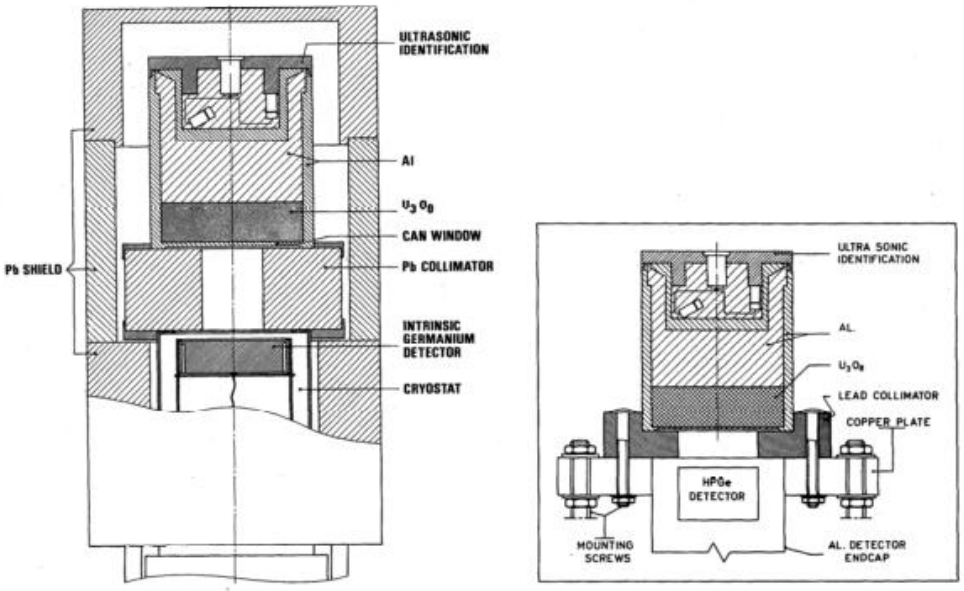

Figure 2. Set-up for Gamma Spectrometry for Counting U_3O_8 Reference Samples a) used by CBNM b) used by NBS

Can dimensions and U_3O_8 mass

Container N° :	NBS 071-078
Tot. Mass U_3O_8 :	(200.1 ± 0.2)g
A :	54.19 mm
B :	11.99
C :	30.00
ϕ_W :	69.88
d :	1.996
H :	88.98
h :	87.00
j :	1.02
ϕ_X :	70.03
ϕ_Y :	66.0
ϕ_Z :	79.97
D :	52.81
E :	20.81
f :	≤0.1

Bottom thickness : 1	2.005 mm
2	1.999
3	2.004
4	2.000
5	2.011
6	2.006
7	2.003
8	2.007
9	1.994
10	1.990
11	1.990
12	1.993
13	2.013
$\bar{x}_{13}$	2.001
$\bar{s}_{13}$	0.008
$\bar{x}_5$	1.996
$\bar{s}_5$	0.010

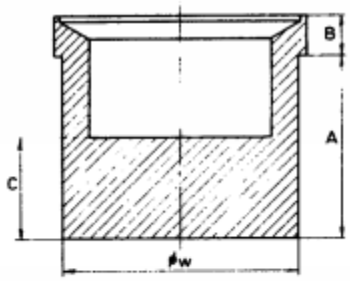

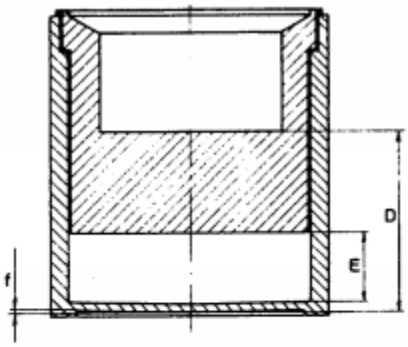

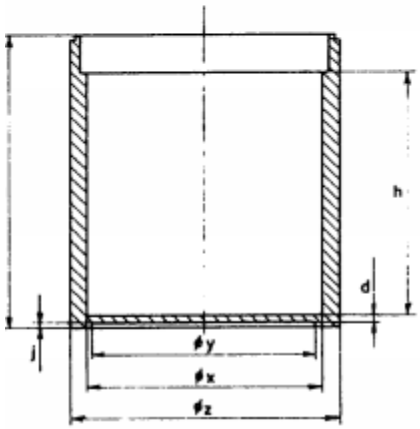

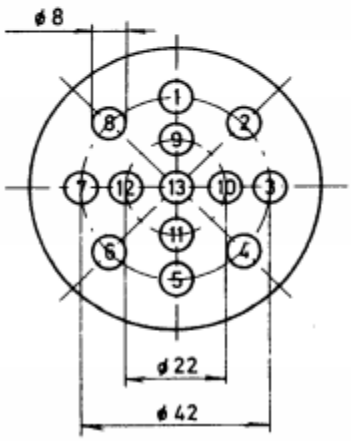

VITA

Name:	Alison Victoria Goodsell
Address:	c/o Dr. William Charlton 336 Zachry Engineering Center Nuclear Security Science & Policy Institute Department of Nuclear Engineering Texas A&M University College Station, TX 77843-3133
Email Address:	alisong@tamu.edu
Education:	B.A., Physics, California Polytechnic State University, San Luis Obispo, 2009 M.S., Nuclear Engineering, Texas A&M University, 2012